

PALEONTOLOGY

Metabolically diverse primordial microbial communities in Earth's oldest seafloor-hydrothermal jasper

Dominic Papineau^{1,2,3,4*}, Zhenbing She¹, Matthew S. Dodd¹, Francesco Iacoviello⁵, John F. Slack^{6,7}, Erik Hauri^{8†}, Paul Shearing⁵, Crispin T. S. Little⁹

The oldest putative fossils occur as hematite filaments and tubes in jasper-carbonate banded iron formations from the 4280- to 3750-Ma Nuvvuagittuq Supracrustal Belt, Québec. If biological in origin, these filaments might have affinities with modern descendants; however, if abiotic, they could indicate complex prebiotic forms on early Earth. Here, we report images of centimeter-size, autochthonous hematite filaments that are pectinate-branching, parallel-aligned, undulated, and containing Fe²⁺-oxides. These microstructures are considered microfossils because of their mineral associations and resemblance to younger microfossils, modern Fe-bacteria from hydrothermal environments, and the experimental products of heated Fe-oxidizing bacteria. Additional clusters of irregular hematite ellipsoids could reflect abiotic processes of silicification, producing similar structures and thus yielding an uncertain origin. Millimeter-sized chalcopyrite grains within the jasper-carbonate rocks have ³⁴S- and ³³S-enrichments consistent with microbial S-disproportionation and an O₂-poor atmosphere. Collectively, the observations suggest a diverse microbial ecosystem on the primordial Earth that may be common on other planetary bodies, including Mars.

INTRODUCTION

Fossils of primordial life or prebiotic and abiotic microstructures?

Ferrous iron oxidation by anoxygenic phototrophs is thought to have been an early evolving metabolism important for the deposition of banded iron formations (BIFs) before the Great Oxidation Event (GOE) (1). Eoarchean BIFs contain magnetite with heavy Fe isotopes consistent with anoxygenic photosynthetic Fe²⁺ oxidation on the early Earth (2, 3). Evidence for the oldest putative microfossils has been reported in a jasper-carbonate BIF from the Nuvvuagittuq Supracrustal Belt (NSB) in the form of hematite filaments and tubes (4). The age of the NSB is still debated, but it is at least 3750 million years (Ma) and possibly as old as 4280 Ma (5, 6). These putative fossils are important for understanding abiogenesis, evolutionary biology, and exobiology. However, the biological interpretation of the NSB filaments (4) has received criticism because some abiotic precipitates can display similar morphologies in highly alkaline solutions (7, 8), such as natural alkaline spring water (9). These “chemical gardens” are self-assembled abiotic biomorphs, or in this case prebiotic and abiotic microstructures that spontaneously precipitated from ionic solutions (10). Ferruginous structures in chemical gardens may also form through diffusion-limited aggregation, which might explain occurrence of the NSB hematite filaments (9–13). Hence, there is a need to revisit such abiotic models as a possible explanation for the recently identified microfossil-like objects in the NSB, such as those reported here.

Questions also remain as to the biogenic origin of phosphorus and sulfur in metamorphically recrystallized minerals such as apatite and chalcopyrite, which occur in the NSB jasper-carbonate BIF. For instance, these rocks also contain millimeter-size chalcopyrite crystals (4) for which S-isotope compositions could inform redox conditions and have implications for biological fractionation. Therefore, measurements of stable isotope composition of sulfur are needed because such data are important for evaluating the presence of biological activity within the context of the oldest putative fossils on Earth.

Geological setting for NSB BIF

Outcrops of NSB jasper-carbonate and Fe-silicate BIF are linearly distributed along strike for more than 3 km within the locally pillowed, 3750-Ma to 4280-Ma Ujaraaluk amphibolite unit (fig. S1A). The BIF is stratigraphically located between a mafic unit of basaltic composition at the base of the sequence and a basaltic to andesitic unit above (14). Jasper-carbonate BIF occurs as orange to red outcrops with irregular white chert bands and red decimeter-size jasper nodules (fig. S1, B and C). This BIF also forms conformable, bedded red jasper with orange carbonate BIF (fig. S1D), and rarely thin beds and veinlets in Fe-silicate BIF (fig. S1E). The jasper-carbonate BIF is interlayered with metavolcanic rocks (fig. S1, F and G) and displays soft-sediment deformation features such as lamina-deflecting nodules of jasper or chert (fig. S1, C, D, and G to I). The jasper-carbonate BIF occurs along strike from the main Fe-silicate BIF unit, which is typically flat-laminated (fig. S1, M to O), but also contains convoluted beds (fig. S1, J to L) and lamina-deflecting diagenetic quartz nodules (fig. S1M). These outcrop features point to deposition in a hydrothermal vent system, fed by siliceous, ferruginous, and carbonized fluids. We emphasize that all of our samples come from stratabound layers and nodules and are not from veins or other late discordant “box-work” structures as claimed in recent studies (15, 16). In this setting, volcanogenic massive sulfide (VMS) deposits might also occur in the NSB, but none has yet been identified. However, the widespread occurrence of cummingtonite and local anthophyllite within the jasper- and BIF-associated “faux” amphibolites (6) is

Copyright © 2022 The Authors, some rights reserved; exclusive licensee American Association for the Advancement of Science. No claim to original U.S. Government Works. Distributed under a Creative Commons Attribution NonCommercial License 4.0 (CC BY-NC).

¹State Key Laboratory of Biogeology and Environmental Geology, School of Earth Sciences, China University of Geosciences, Wuhan, China. ²London Centre for Nanotechnology, University College London, London, UK. ³Department of Earth Sciences, University College London, London, UK. ⁴Centre for Planetary Sciences, University College London & Birkbeck College London, London, UK. ⁵Department of Chemical Engineering, University College London, London, UK. ⁶U.S. Geological Survey National Center, Reston, VA, USA. ⁷Department of Earth Sciences, Memorial University of Newfoundland, St. John's, NL, Canada. ⁸Department of Terrestrial Magnetism, Carnegie Institution for Science, Washington, DC, USA. ⁹School of Earth and Environment, University of Leeds, Leeds, UK.

*Corresponding author. Email: d.papineau@ucl.ac.uk
†Deceased.

similar to the cummingtonite- and anthophyllite-rich amphibolites that host some ancient VMS deposits (17). Premetamorphic alteration of basalt by VMS-related hydrothermal fluids typically leaches most Ca and Na, which together with the introduction of abundant Mg (from evolved seawater) produces bulk compositions that during regional metamorphism generate cummingtonite + anthophyllite ± cordierite ± garnet instead of typical hornblende + plagioclase in unaltered basalt. However, the high grade of metamorphism endured by all NSB rocks possibly prevents the preservation of most primary mineral textures and delicate syn-sedimentary structures. A high-resolution geological map of the area remains to be produced to establish the detailed nature of this paleoenvironment through mapped field relationships.

RESULTS

Unprecedented observations of NSB pectinate-branching filaments and irregular ellipsoids

New petrographic thin sections of jasper nodules from the NSB jasper-carbonate BIF (fig. S2, A to C) reveal centimeter-size, pectinate-branching bundles of parallel-aligned hematite filaments, each hundreds of micrometers in length (Fig. 1, A and B, and fig. S3). The previously unidentified pectinate-branching structure appears to stem from a main filament and occurs near the center of jasper nodules, from which filaments and tubes have been documented previously (4). The morphology of hematite filaments varies from straight to undulated or coiled (fig. S4, A to K), and those in pectinate-branching arrangement (oriented toward one main direction) have an average diameter of $16.5 \pm 5 \mu\text{m}$ (1σ ; $n = 53$), which is larger by a factor of 2 compared to the range of diameters previously reported for singular hematite filaments from the NSB (4). Some straight filaments contain periodically spaced crystals along their lengths (fig. S4J), consistent with the presence of small-amplitude undulations. Undulated hematite filaments have a short period of up to $30 \mu\text{m}$ (fig. S4, F to H, SV1 and SV2) or a longer undulation period of up to $100 \mu\text{m}$ (fig. S4, I to K, SV3 and SV4). Recrystallization during metamorphism clearly produced some coarse hematite grains and distortions of many hematite filaments. Notable features directly associated with parallel-aligned filaments (fig. S3) include (i) previously unrecognized clusters of microscopic “irregular ellipsoids” (Fig. 1, C and D, and fig. S4, B and O, SV5); (ii) concentrically layered hematite rosettes (fig. S4, B to F); (iii) millimeter-size, recrystallized, subhedral apatite and calcite crystals (Fig. 2, A to C, and fig. S4, L and M); and (iv) tubular structures (fig. S4, D, F, G, and I). Cross-polarized light microscopy images clearly show that irregular spheroids, parallel-aligned filaments, and cylindrical tubes of nanoscopic hematite occur within both fine and coarse-grained quartz, although fine (cryptocrystalline) quartz has a higher fidelity of preservation for filaments and ellipsoids than coarse quartz. For instance, in coarse quartz, the irregular spheroids are commonly fused, tubes have more varied widths, and filaments are more blocky, whereas the opposite is observed in fine quartz where individual microstructures are less deformed (fig. S5, A to G). An x-ray-based tomographic reconstruction of two 2-mm-long, parallel-aligned filaments demonstrates undulated to coiled microstructures (fig. S6A, SV6). Another tomographic reconstruction based on ion milling and backscattered electron (BSE) imaging independently confirms the presence of an undulated morphology and additionally shows the nanoscale mineralogy of the NSB filaments (Fig. 1F and fig. S6, B to D, SV7).

Filaments commonly have heterogeneous intracrystalline domains of Fe^{2+} -bearing hematite, the presence of ferrous iron indicated by a small Raman peak at 668 cm^{-1} (fig. S4N). This result is consistent with two shades of light gray observed in BSE images of cross-sectioned undulated hematite filaments (Fig. 1F), which also commonly contain nanoscopic coatings of graphitic carbon and nanoscopic rounded inclusions of quartz (Fig. 1F). Trace graphitic carbon mixed with hematite defines the contour of undulations in three dimensions (fig. S6, C and D). We note the presence of hematite and graphitic carbon uncorrelated to the main targeted undulated filament (fig. S6C); however, these regions represent a second underlying filament partly in the same plane as the main targeted filament (fig. S6B). Transmitted light images show two filaments. In any case, the main filament is composed of nanoscopic to micrometer-size hematite crystals mixed with graphitic carbon. They are also comparable to those of mixed ferric-ferrous oxides produced in diagenetic experiments on modern stalks of Fe-oxidizing bacteria (fig. S4N) (18), as well as to observations by energy-dispersive spectroscopy of trace levels of C and P inside Fe-oxide microbial filaments from the modern Jan Mayen hydrothermal vents (12).

Diagenetic granules of coarse recrystallized quartz are associated with pectinate-branching filament bundles and contain clusters of dozens of microscopic, irregular ellipsoids with walls composed of nanoscopic hematite (Fig. 1C and fig. S4B). These irregular ellipsoids ($n = 319$) have an average size of $20.5 \pm 4.8 \mu\text{m}$ (1σ) and an average aspect ratio (long length divided by short length) of 1.3 ± 0.2 (1σ) (Fig. 1G, SV2 to SV5). The irregular ellipsoids commonly occur in groups, typically linear and oriented parallel with the filaments, but are not uniformly associated with parallel-aligned filaments (fig. S4O). The irregular ellipsoids are also distinctively smaller, simpler, with more irregular shapes, and more populous than the hematite rosettes. However, the irregular ellipsoids are not recrystallized coated grains because the chert within and surrounding them has the same uniform texture in cross-polars. The ellipsoids are also more perfectly rounded, where present in fine-grained quartz compared to coarse quartz (fig. S5, C and F). Hematite rosettes are rather widely distributed among filaments (Fig. 1, A and B, and fig. S4, C to F) and display at least two sets of concentric rings of hematite and quartz (4), as opposed to a single ring as seen in the irregular ellipsoids. Cross-polar images of rosettes also show radially aligned quartz crystals. Rosettes co-occur with organic matter and filaments, and are morphologically and compositionally similar to younger diagenetic rosettes within seafloor-hydrothermal jasper from other localities (19, 20). There is also a third rarer type of “discrete spheroid” ($n = 2$), about 80 to $90 \mu\text{m}$ in diameter and having a coarser hematite outer wall and filamentous hematite in the center (fig. S4P, SV8). Hence, at least three types of hematite spheroidal microstructures exist in the NSB jasper- BIF, distinguishable as (i) diagenetic rosettes with concentrically layered hematite, (ii) irregular ellipsoids of hematite occurring as clusters, and (iii) discrete hematite spheroids with a complex internal structure. Pectinate-branching hematite filaments and irregular ellipsoids thus occur with diagenetic minerals that grew coarser in size during metamorphism while preserving some original microfossil-like textures, thus making these microstructures at least dubiofossils of uncertain origin.

Trace element and rare earth element compositions of NSB BIF

Bulk analyses of trace metals (Fig. 3A and Table 1) reveal overlapping ranges of concentrations for the Fe-silicate and the jasper-carbonate

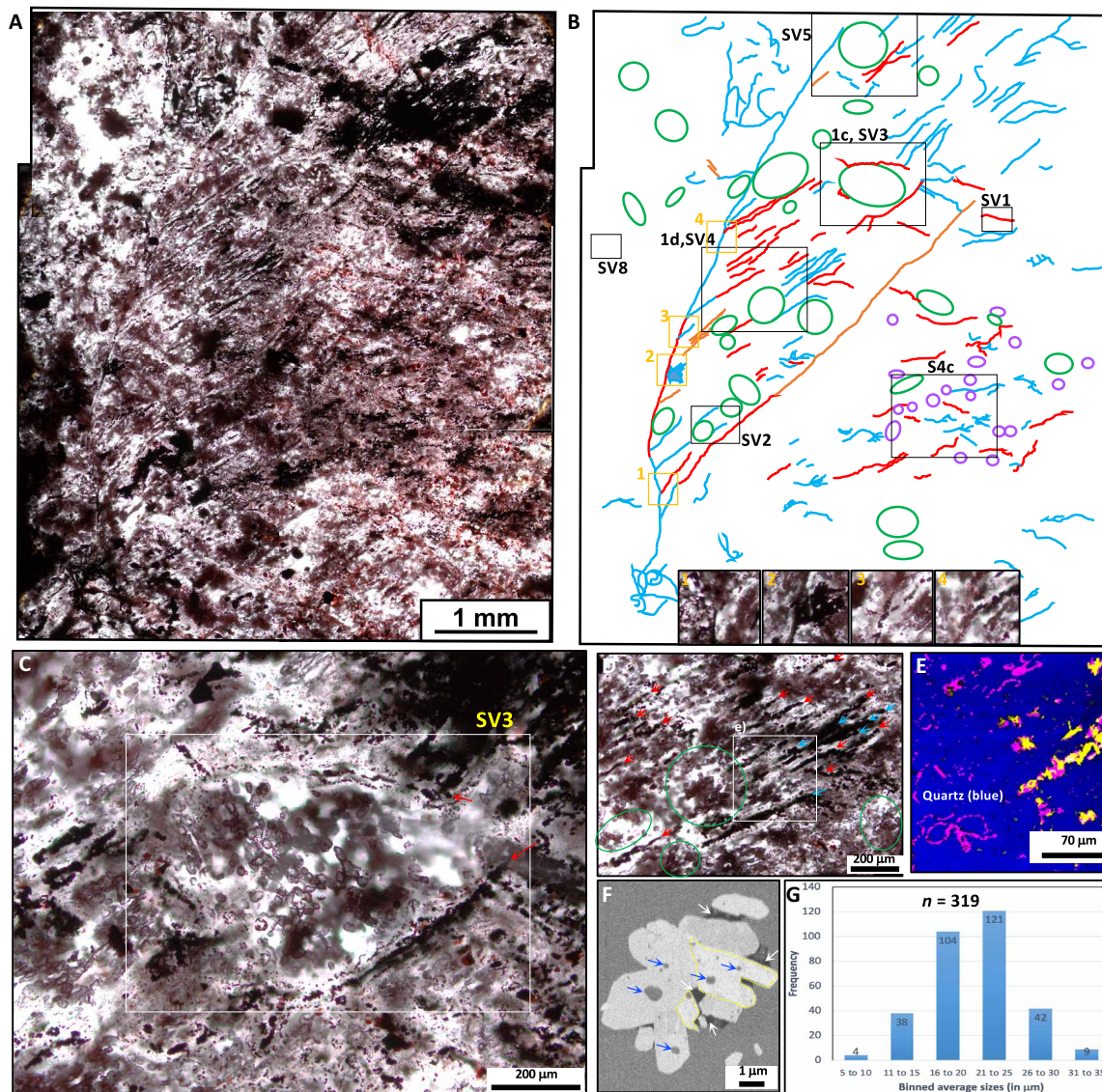


Fig. 1. Hematite filaments and spheroids in NSB jasper-carbonate BIF. (A) Transmitted light image of a bundles of pectinate-branching hematite filaments with undulations and tubes and co-occurring clusters of irregular ellipsoids. (B) Corresponding interpretive drawing showing straight filaments (blue lines), undulated or coiled filaments (red lines), tubes (orange lines), rosettes (purple circles), clusters of irregular ellipsoids (green ovals), and areas for other figure panels and videos. The four photos in inset show four examples of branching filament intersections in this structure. (C) Cluster of irregular ellipsoids inside a coarse quartz granule rimmed by two undulated filaments (red arrows). (D) Parallel-aligned hematite filaments and associated irregular ellipsoids. (E) Raman image showing a filament with coarse Fe^{2+} -bearing hematite (yellow) and hematite (purple) (spectra shown in fig. S4N). (F) BSE image of a cross-sectioned undulated filament (shown in fig. S4K) with graphitic carbon (white arrows) associated with ferrous hematite (yellow contour) and quartz inclusions (blue arrows). (G) Histogram of the sizes of the irregular ellipsoids (average of major and minor axes).

BIF. Elements phosphorus (P), manganese (Mn), vanadium (V), and titanium (Ti) are often above 100 parts per million (ppm), while elements zinc (Zn), cobalt (Co), and nickel (Ni) are typically between 10 and 100 ppm. Element molybdenum (Mo) is detectable above 1 ppm and below 10 ppm, while cadmium (Cd) is below 1 ppm and copper (Cu) was not detected. The lack of detectable Cu also occurs in the jasper-carbonate BIF despite it containing millimeter crystals of chalcopyrite. This can be explained by its highly heterogeneous petrologic mode of occurrence. Briefly, the trace metal profile from the NSB is similar to that in the early Paleoproterozoic Dales Gorge BIF from Western Australia.

Data for rare earth elements (REEs) and Y in the NSB jasper-carbonate BIF are presented in table S1. Shale-normalized REE + Y concentrations (Fig. 3B) show total abundances of $\sim 0.01\times$ to $\sim 1\times$ average post-Archean Australian shale (PAAS), low La/Yb ratios, and positive Eu and Y anomalies. Similar REE abundances, La/Yb ratios, and Eu anomalies are shown by the NSB Fe-silicate BIF and associated stratabound lithologies including amphibolite and calc-silicate rock; Y anomalies are small or absent (fig. S7, A and B). For comparison, many modern Si-Fe hydrothermal solid phases and some modern seafloor-hydrothermal fluids have broadly similar REE patterns including positive Eu and Y anomalies (fig. S7, C and D). A discriminant plot

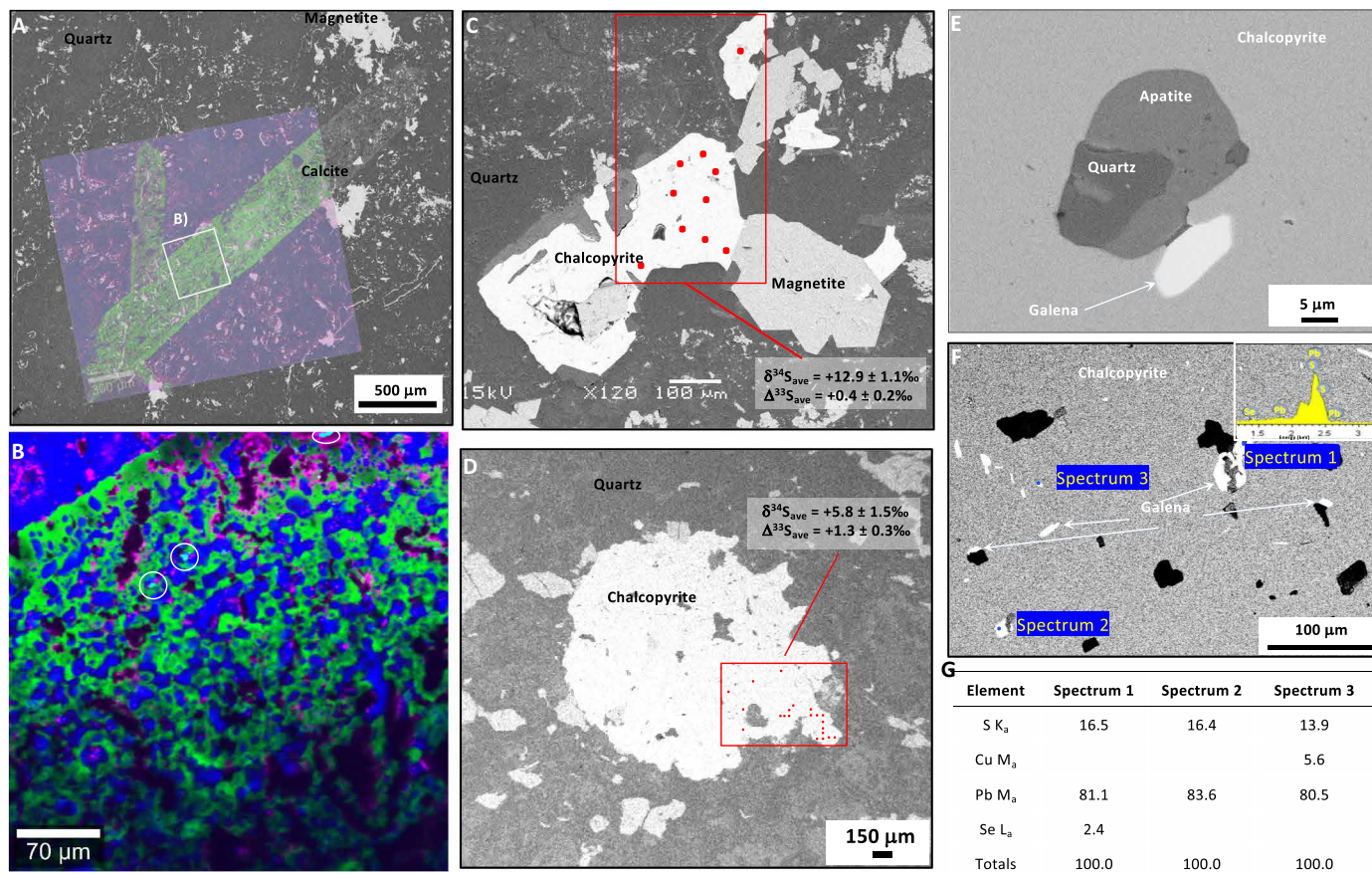


Fig. 2. Petrography of outsized calcite and chalcopyrite in jasper-carbonate BIF. (A and B) Visually correlated Raman-SEM (scanning electron microscopy) images (in BSEs) of cross-cutting millimeter-size calcite laths with a recrystallized texture of collapsed rosettes with apatite inclusions (white circles) (PC0822). Colors in the micro-Raman images are as follows: blue for quartz, green for carbonate, purple for hematite, and turquoise for apatite. (C and D) Outsized subhedral chalcopyrite crystals with ^{34}S - and ^{33}S -enrichments (spot analyses shown as small red dots and averages with one SD specified), associated with magnetite (PC0824). The chalcopyrite in PC0844 has inclusions of (E) apatite-quartz in direct contact with galena and (F) of micrometer-size euhedral to anhedral galena (white), including with selenium enrichments as shown in spectrum in inset and in (G) table of three energy-dispersive spectroscopic analyses.

of PAAS-normalized Ce anomalies (Ce/Ce^*) versus Pr anomalies (Pr/Pr^*) indicates that most NSB rocks have positive La anomalies; only one valid negative Ce anomaly and one valid positive Ce anomaly are evident, each for samples of Fe-silicate BIF (fig. S7E). Calculated PAAS-normalized La/Yb ratios of the jasper-carbonate and Fe-silicate BIF are all <0.7 , like those of the NSB amphibolite and calc-silicate rocks, as are calculated Eu anomalies (Eu/Eu^*) and Y/Ho ratios (fig. S7, G and H). The uniformly positive Eu and Y anomalies (Fig. 3B and fig. S7, G and H) present in the jasper-carbonate BIF are consistent with analyses of NSB apatite grains (4) and the NSB Fe-silicate BIF (Fig. 3B and fig. S7A).

Multiple sulfur isotope composition of sulfides in the NSB

Results of the multiple sulfur isotope data presented in this work are self-consistent between the two techniques used (table S5). Nanoscale secondary ion mass spectrometry (NanoSIMS) data on different sulfide crystals from the same samples tend to show larger ranges of delta values [defined as $\delta^{34}\text{S} = (((^{34}\text{S}/^{32}\text{S})_{\text{sample}} / (^{34}\text{S}/^{32}\text{S})_{\text{CDT}} - 1) \times 1000\text{‰})$] than by isotope ratio mass spectrometry (IRMS), although both datasets were independently produced and overlap in both $\delta^{34}\text{S}$

and $\Delta^{33}\text{S}$ values [Fig. 4B; where $\Delta^{33}\text{S} = 1000 \cdot ((1 + \delta^{33}\text{S}/1000) - (1 + \delta^{34}\text{S}/1000)^{1/2})$]. These analytically redundant analyses were performed on chalcopyrite, pyrite, and pyrrhotite by NanoSIMS ($n = 92$) (Fig. 4, fig. S8, and table S3, A and B) (21) and by IRMS ($n = 42$) (Fig. 4, fig. S9, and tables S4, A and B, and S5) (22) on microdrilled powders of sulfides from the same rock slabs used for thin sectioning and subsequent microscopy. Amphibolitic metavolcanic rocks of the NSB associated or interbedded with Fe-silicate BIF contain pyrite with mass independently fractionated (MIF) $\Delta^{33}\text{S}$ values of ca. $+1.8\text{‰}$, but with $\delta^{34}\text{S}$ values between -1.0 and 0.0‰ . Sulfides in Fe-silicate BIF display a similar range of positive and negative enrichments of ^{33}S with $\Delta^{33}\text{S}$ values of -0.9 to $+3.3\text{‰}$, but a small range of $\delta^{34}\text{S}$ values between -5.7 and $+2.3\text{‰}$ (table S3), similar to previously reported analyses of sulfides in Fe-silicate BIF from the NSB (Fig. 4 and fig. S8) (23, 24). In contrast, outsized chalcopyrite crystals in the NSB jasper-carbonate BIF have multiple sulfur isotope compositions that reveal both MIF and mass-dependent fractionation (MDF) (fig. S8 and table S3) with positive $\Delta^{33}\text{S}$ values between $+0.1$ and $+2.0\text{‰}$, and $\delta^{34}\text{S}$ values of $+2.9$ to $+14.6\text{‰}$, the latter being notably ^{34}S -enriched.

Table 1. List of independent lines of evidence for habitability and biosignatures in the NSB jasper-carbonate BIF, with new observations from this work shown in *italics*. The term “biosignature” is defined in this work as a “possible evidence of life.” This list includes both biological and abiotic features involved in the carbon cycle. In this case, “abiotic biosignatures” are those that are interpreted to involve both abiotic processes and the decomposition of biomass.

Habitability of the depositional environment

- *Hydrothermal vent type of depositional environment inferred from rock types, field relationships, and REE**
- Host rock is jasper-carbonate BIF, known to locally contain filamentous microfossils (41)
- Presence of BIF and pillowed amphibolite point to a seafloor-hydrothermal environment (6)
- Occurrences of jasper and ankerite veins in amphibolite record fluid circulation in the basaltic seafloor (102)
- Presence of inosilicate and phyllosilicate minerals in BIF points to prograde and retrograde metamorphic reactions (4)
- *Chalcopyrite from jasper with $\Delta^{33}\text{S}$ between +0.1 and +2.0‰ interpreted to indicate anoxic to microaerophilic conditions**
- *REE data show positive Eu and Y anomalies, consistent with data for younger jasper BIF and modern hydrothermal vent environments (4)**
- *Trace metal enrichments observed for V, Ba, Mn, Ni, Zn, Co, and Mo**

Mineralogical and sedimentological abiotic biosignatures

- Granules contain ferric-ferrous oxides, apatite, calcite, and graphitic carbon (4)
- *Chert granules with clusters of microscopic spheroids occur inside pectinate-branching hematite filaments**
- Calcite-ankerite rosettes have concentric rings of micrometer-size quartz (4)
- Calcite-ankerite rosettes contain inclusions of apatite and graphitic carbon and cores of quartz (4)*
- *Rosettes of hematite have two or more concentric rings and occur in clear quartz and are interpreted as pseudofossils (4)**
- Millimeter-size apatite crystals occur with inclusions of graphite, carbonate, quartz, and fluids (4)
- Presence of oversized crystals of recrystallized diagenetic apatite and chalcopyrite (4)*
- *Centimeter- to decimeter-sized nodules of jasper contain millimeter-sized laths of calcite with rosette texture**
- *Inclusions of apatite with metamorphic galena occur in oversized chalcopyrite**

Geochemical biosignatures

- Total graphitic carbon content varies between 0.004 and 0.034 weight % (72)
- $\delta^{13}\text{C}$ values of bulk graphitic carbon are -20.4 to -24.0 ‰ (72)
- $\delta^{13}\text{C}$ values of bulk carbonate are -2.2 to -6.1 ‰ (72)
- $\delta^{34}\text{S}$ values of chalcopyrite are between $+2.9$ and $+14.6$ ‰*

Paleontological biosignatures: microfossils and dubiofossils

- Organized and morphologically complex microstructures dominantly occur inside jasper nodules (4)*
- Filaments attached to hematite terminal knobs interpreted as microfossils (4)
- Filaments associated with micrometer-size carbonate, apatite, and graphitic carbon interpreted as microfossils (4)*
- Tightly undulated to coiled filaments of hematite interpreted as microfossils (4)*
- Loosely undulated to coiled filaments of hematite interpreted as microfossils (4)*
- *Filaments composed of ferrous and ferric oxides interpreted as microfossils**
- *Poikilotopic texture inside hematite filaments interpreted as microfossils, with quartz and graphitic carbon inclusions**
- Microscopic tubes of nanoscopic hematite with and without filaments interpreted as dubiofossils (4)
- *Centimeter-long clusters of pectinate-branching and parallel-aligned filaments interpreted as microfossils**
- *Three types of spheroids, interpreted as dubiofossils or pseudofossil, associated with hematite filament bundles**
- *Clusters of microscopic irregular ellipsoids, interpreted as dubiofossils with walls of nanoscopic hematite**

*This work.

DISCUSSION

Evaluation of possible abiotic origins for the microstructures

To be interpretable as possible signs of life, abiotic reactions need to be discounted as origins for the newly recognized filaments and irregular ellipsoids (7, 8). Furthermore, it must also be demonstrated that these microstructures originated within the depositional

environment and did not form during later processes. First, the primary premetamorphic origin of the filaments and irregular ellipsoids in the jasper-carbonate BIF is confirmed by their common occurrence within various diagenetic structures: (i) inside centimeter-size, layer-deflecting jasper nodules (figs. S1, H and I, and S2, A to C); (ii) within submillimeter granules composed of coarse quartz (Fig. 1C); and

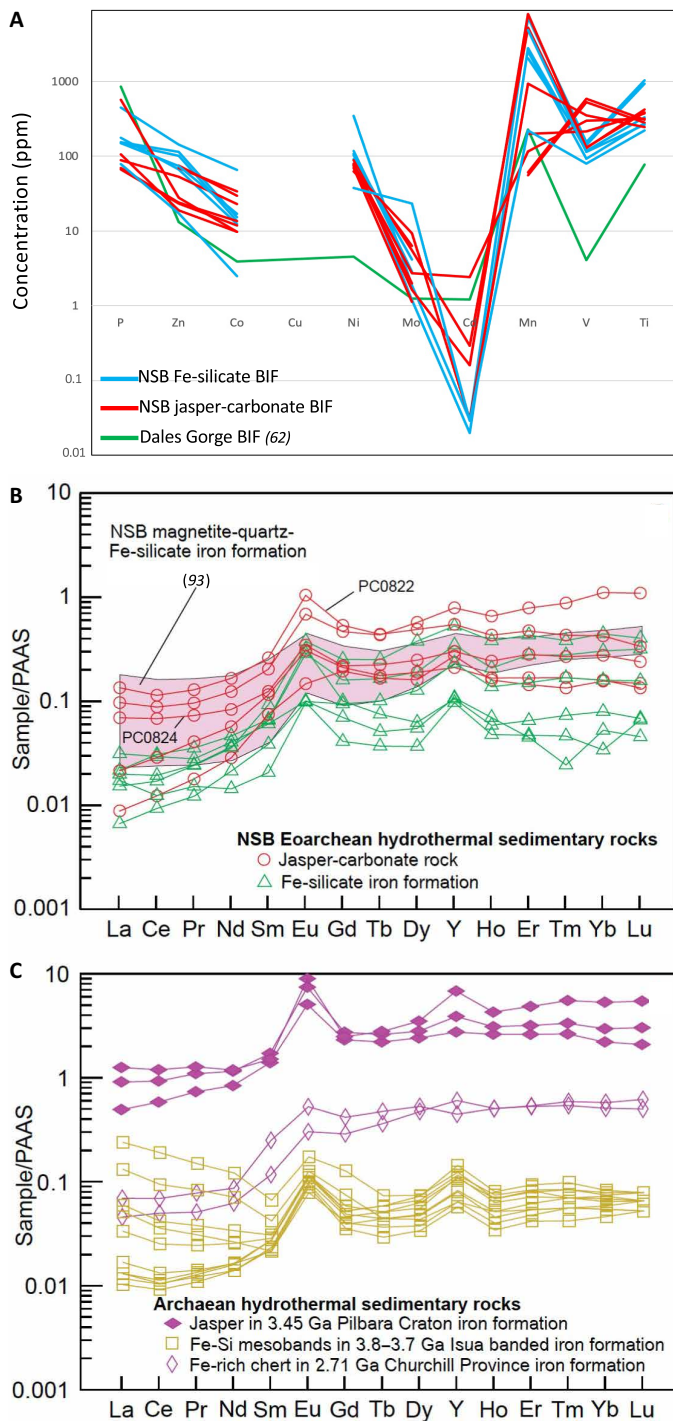


Fig. 3. Trace element and rare earth element plots for NSB Fe-silicate BIF and jasper-carbonate BIF. (A) Trace metals and phosphorus profile for NSB BIF (red is jasper-carbonate BIF and blue is Fe-silicate BIF) compared to Dales Gorge average [green; data from (62)]. New data are shown in table S1. (B) REE plots of hydrothermal sedimentary rocks of the NSB; data are from this study (table S1) and (93), normalized to average post-Archean Australian shale [PAAS; (99)]. (C) For comparison, Archean hydrothermal jasper and Fe-rich chert; data are from (53), (84), and (85).

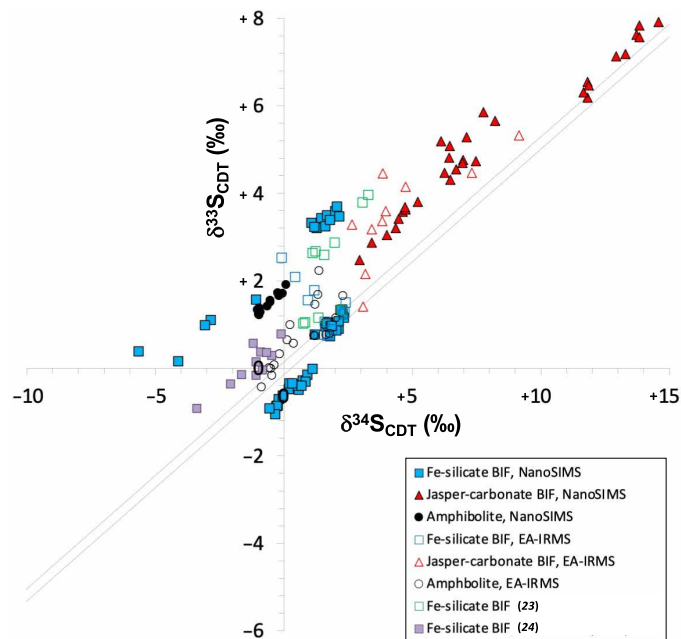


Fig. 4. Three sulfur isotope plot for NSB sulfide minerals based on NanoSIMS and EA-IRMS analyses. Chalcopyrite in the jasper-carbonate BIF (red triangles) compared to pyrite and pyrrhotite in the Fe-silicate BIF (blue squares). Filled symbols are NanoSIMS spot analyses; open symbols are IRMS analyses of drilled powders. Comparison with other sulfur isotope compositions from NSB Fe-silicate BIF is shown. Detailed data are shown in the Supplementary Materials, and the data with green open squares and purple filled squares are from (23) and (24).

(iii) nearby microscopic circularly concentric rosettes with radially aligned quartz (figs. S4, B to F, and S5H). Abiotic chemically oscillating reactions during the early diagenetic oxidation of organic matter can partly explain the formation of these nodules, granules, and rosettes (25–27). This interpretation stems from the similar, circularly concentric patterns that radially expand during redox reactions involving C, S, and Fe, such as the Belousov-Zhabotinsky reaction (28), and that may be preserved in mineral compositions (29). Second, the variable preservation of filaments as coarse- to fine-grained hematite, combined with the higher fidelity of their preservation as less-deformed and parallel-aligned filaments within fine-grained quartz (figs. S4, G to K, and S5, E and G), is an observation consistent with recrystallization during metamorphism. Third, the NSB filaments and spheruloids could conceivably have formed as abiotic chemical gardens, for instance, from diffusion-limited aggregation as abiotic dendritic growths or self-assembly akin to microstructures of filamentous agate moss. As with most chemical gardens, such growth is expected to require alkalinity where abiotically grown mineral structures are later replaced geologically and abiotically by hematite (9, 30, 31).

Abiotic biomorphs of twisted filaments similar to the NSB filament bundles have been made in other studies experimentally using barium, strontium, and calcium carbonate under alkaline conditions (7, 8). A review of comparable abiotic filamentous biomorphs to the NSB filaments is done here based on size, morphology, and plausible precursor chemical compositions (fig. S10). Abiotic biomorphs have morphologies of disordered filaments, twisted ribbons, thin sheets, irregular and outward-branching filaments, dendritic growths, and nanorods containing aligned nanocrystals (fig. S10, A to C) (9, 32). However, all of these abiotic biomorphs differ from our newly observed

NSB pectinate-branching filaments that have a smaller range of diameters, undulated to coiled morphologies, and a more organized distribution as pectinate-branching and occurrence in parallel alignment. Chemical garden experiments with silica-sulfate-phosphate solutions can produce hollow plumes, bulbs, and amorphous to straight tubes, which have highly variable diameters (fig. S10D) (30). Filamentous abiotic biomorphs of fatty acids can also spontaneously self-assemble under alkaline conditions (fig. S10E) (33), but these do not display organized orientations. Slightly more organized groups of abiotic filaments can be produced by oxidizing solutions of mixed complex organics and sulfide (fig. S10F) (34), but these reactions require abundant oxygen and are thus improbable for the Early Archean ocean. Experiments with Co- and Mn-chloride yield the precipitation of aligned microtubes that can be straight to coiled (fig. S10G), although not well-organized like the NSB filaments (35). The NSB jasper-carbonate BIF contains Mn and Ba concentrations up to 0.8 and 0.001 weight %, respectively, less than 34-ppm Co, and relatively high levels of P and Ni, comparable to those in Fe-silicate BIF (Fig. 3A and table S1); therefore, a model involving the partial replacement of silica-witherite or metalliferous abiotic biomorphic filaments by hematite might be possible. Whereas such reactions are plausible in the NSB depositional environment, which may have been locally alkaline, abiotic biomorphs of silica, witherite, barium carbonate, and metals are not known to include complex, organized bundles of parallel-aligned undulated hematite filaments decorated by tubes and clusters of microscopic irregular ellipsoids, as occur in the NSB samples.

Alkaline to neutral-pH ferruginous chemical gardens can also produce filaments morphologically similar to those of the NSB hematite filaments (fig. S10H). These include tubes with a variable range and smaller diameters, tubes that flare out and have filled or unfilled interiors, attachments to ferruginous particles, and multiple branching points (13). Here again, however, none of these experiments has produced parallel-aligned, undulated filaments inside tubes with pectinate-branching growths that co-occur with clusters of irregular ellipsoids. Abiotic dendritic-type mineralization with arborescent structures composed of Mn and Fe oxides such as agate moss and mocha stones (fig. S10I) (36) is also morphologically distinct from the NSB pectinate filaments, as the former have dendritic bilateral branches, highly variable branch diameters, and bulbous terminations. However, modern pectinate-branching filament bundles have been described in the context of deep-sea hematite branching structures from the Jan Mayen hydrothermal vent field and interpreted as the result of Saffman-Taylor instability and diffusion-limited aggregation (12, 32). Ambiguous and undemonstrated arguments have been made that the strict parallel alignment of tubes, the presence of dendrites, and four-way branching points suggest abiotically controlled precipitation (12). Whereas abiotic experiments show potential to explain some simple features of the NSB filament bundles, none of these purported abiotic features is observed in the NSB jasper-carbonate BIF. Hence, the NSB hematite filaments do not fit observations of known chemical gardens, and although some abiotic processes can explain some individual microstructures, abiotic chemical gardens are not yet known to reproduce the full range of ferruginous pectinate-branching and parallel-aligned filaments reported here. It remains that our knowledge of abiotic biomorphs is somewhat limited, with most examples having been discovered by accident; thus, future variants of experiments using geologically relevant chemical compounds might be able to explain more or all of the NSB features. Consequently, we cannot completely exclude the possibility that all

of the NSB microstructures are pseudofossils, and hence that are all abiotic. However, before such an interpretation can be rigorously supported, quantitative abiotic experiments will need to reproduce more of the complex microstructures observed within the NSB jasper-carbonate BIF (Table 1).

The NSB irregular ellipsoids share some similarities with known spheroidal abiotic biomorphs made of silica-witherite, which can also be oblate but not with those composed of barium carbonate, proto-dolomite, or organic acids. The spontaneous precipitation of spheroids composed of colloidal silica, barium carbonate, proto-dolomite, or witherite produces mostly spheroids (fig. S11, A to D) (9, 37, 38), with an aspect ratio of about 1, although only a few abiotic biomorphs of silica-witherite form irregular ellipsoids (fig. S11B). Abiotic biomorphic spheres have well-sorted sizes that range in diameter from a few tens of nanometers to tens of micrometers and can be organized in clusters or layers. However, their sphericity is generally distinct from those of the NSB irregular ellipsoids, which have an average aspect ratio of 1.3 ± 0.2 ($n = 309$). Moreover, the ellipsoids encased in fine-grained quartz lack preferential orientation, compaction, or deformation; thus, metamorphism can be excluded as a cause of their oblateness. This distinction based on sphericity is also applicable to abiotic biomorphs made from organic acids, such as chemical oscillations that produce various self-similar, circularly concentric patterns during the oxidation of carboxylic acid (fig. S11E) (39), and the self-assembly of spherical vesicles of fatty acids from meteorites or mixed solutions [fig. S11, F and G; (33, 40)]. Vesicles self-assembled from amphiphilic molecules can also produce teardrop shapes and spheroids having various diameters (33, 40), but these are also poorly sorted in size and lack the unimodal size distribution of the NSB irregular ellipsoids. Therefore, because some chemical gardens of silica-witherite can produce clusters of irregular ellipsoids with a comparable size distribution, we classify the NSB irregular spheroids as dubiofossils. Regardless, although chemical gardens can generate pseudofossils similar to some NSB microstructures, including filaments and tubes of Fe-oxides and spheroids of silica-carbonate, these remain poorly understood. More work is needed to determine whether chemical gardens can produce pseudofossils like all of those documented in the NSB specimens and provide criteria for how to unambiguously recognize an abiotic signature. Hence, on balance, we conservatively interpret the irregular ellipsoids and clusters they form as dubiofossils, although in light of the above uniformitarian comparisons, the NSB pectinate-branching and parallel-aligned hematite filaments are most parsimoniously interpreted as biological in origin.

Uniformitarian comparisons with the NSB microstructures

Comparisons with hematite filament bundles in younger jasper (fig. S12) show that the NSB pectinate filaments have a similar organization, lengths and diameters, and undulations. For instance, comparable pectinate-branching hematite filaments occur in various Phanerozoic and Paleoproterozoic jaspers (fig. S12 and table S2), all of which are interpreted as microbial in origin, on the basis of Fe-redox chemistry under an inferred redoxcline (41). In modern seafloor-hydrothermal environments from the Arctic, Pacific, and Indian oceans, some microstructures are made of Fe-oxides within siliceous mounds near hydrothermal vents, having similar morphologies, sizes, and chemical compositions as the NSB specimens (fig. S13). Sheaths, twisted filaments, extensive bacterial mats, and branching, bunched, and braided filaments from the Loihi and Franklin seamounts have been

interpreted as benthic microbial filament bundles made of ferric-ferrous oxides (fig. S13) (42, 43). Morphologically similar modern hydrothermal vent-hosted Fe-oxidizing bacteria are also notable, such as those occurring in bundles of pectinate-branching and parallel-aligned filaments with twisted stalks from hydrothermal vents on Loihi and Edwards seamounts, although these examples are smaller by about one order of magnitude in size than those from the NSB (fig. S13, B and C) (12, 44, 45). However, other modern specimens of filament bundles and parallel-aligned filaments have been reported from the Loihi seamount and Jan Mayen island volcano, all of which share close similarities in contents of abundant Fe-oxides, presence of local pectinate-branching or parallel-aligned textures, as well as comparable lengths and diameters (fig. S13, A and D) (12, 44). In addition, occurrences of carbonate-apatite and graphitic carbon associated with the NSB hematite filaments (Fig. 1F and fig. S4, L and M) (4) are also consistent with visually correlated mapping of elevated carbon, phosphorus, and sulfur concentrations within biogenic hematite filaments compared to those from modern marine hydrothermal sites (12). The presence of euhedral, recrystallized Fe²⁺-bearing hematite and graphitic carbon inside hematite filaments is also consistent with the metamorphic recrystallization of similar diagenetically altered biogenic filaments (18). However, the presence of carbonaceous material in chemical sedimentary rocks associated with hydrothermal vent systems is not surprising because abiotic hydrocarbons were essential to the origin of life and are commonly observed in modern hydrothermal systems (46). Furthermore, Fe-oxide filaments on Franklin Seamount co-occur with aggregates of irregular spheroids that have been interpreted as possibly abiotic (43).

The NSB irregular ellipsoids also resemble younger microfossils and modern bacteria. For instance, some Paleoproterozoic cherts contain irregular ellipsoids with silicified walls composed partly of organic matter and display similar morphologies and sizes as the NSB occurrences (fig. S14, A and B) (47, 48). Irregular ellipsoids in late Paleoproterozoic jasper are smaller but have a comparable morphology (49) (fig. S14C), whereas those from Neoproterozoic cherts are both similar in size and morphology to the NSB irregular ellipsoids (fig. S14D) (50). Comparisons with plausible modern analogs including bacillus-shaped, anoxygenic phototrophs, and Fe-oxidizers (fig. S15) show that the purple sulfur bacterium *Chromatium okenii* (fig. S15C) is morphologically most similar and comparable in size to the NSB irregular ellipsoids. We thus speculate that anoxygenic photosynthesis, possibly harvesting infrared radiation emitted from hydrothermal vents (51), or simply from within the photic zone, could be responsible for the linear arrangement of the clusters of irregular ellipsoids associated with pectinate-branching filaments in the NSB. To sum up, all of the characteristics of the NSB pectinate-branching filaments and some of the irregular ellipsoids can be found in younger seafloor-hydrothermal jaspers and cherts, and in analogous environments. Our interpretations of the pectinate-branching filaments as microfossils are based on inferences from polarized light microscopic images that show parallel-aligned filaments and the best preservation inside tubes contained within fine-grained quartz. The clusters of irregular ellipsoids are more enigmatic but resemble microfossils from the Paleoproterozoic Strelley Pool Chert for which a biological origin was argued on the basis of putative carbonaceous septa interpreted to have arisen from the constriction of cellular compartments (47). However, to our knowledge, there are no known modern microbial communities that form pectinate-branching growths of parallel-aligned and undulated filaments inside tubes that also

co-occur with clusters of irregular ellipsoids, and hence, comparisons with modern microorganisms are imperfect. Moreover, the notable recrystallization of quartz from cryptocrystalline to coarse submillimeter grains blurs the exact mechanism of fossilization and exact nature of the original forms. While some uncertainties still exist, such as the lack of younger or modern microbial communities identical to those preserved in the NSB jasper-carbonate BIF and to the dubiofossils of irregular ellipsoids, similarities between the NSB pectinate-branching hematite filaments and younger to modern seafloor-hydrothermal pectinate-branching filamentous microbial communities lead to the conclusion that the NSB filaments are biological in origin.

Seafloor-hydrothermal depositional environment

Data for REE and Y in the NSB jasper-carbonate BIF (table S1) inform the environmental conditions during deposition. Important insights come from uniformly positive Eu and Y anomalies for this rock and the NSB Fe-silicate iron formation (Fig. 3B and fig. S7F). Similar anomalies are evident for other Archean BIF from the Isua Supracrustal Belt in West Greenland, the Pilbara Craton in Western Australia, and the Churchill Province in northern Canada (Fig. 3C), and for some modern Si-Fe hydrothermal sediments and low-temperature fluids (fig. S7, C and D). The data for Eu anomalies (Eu/Eu*) and Y/Ho ratios are collectively interpreted to reflect variable mixtures of three principal components: seawater, high-temperature hydrothermal fluid, and local mafic igneous crust (using NSB gabbros as a proxy; fig. S7F). REE data for the NSB rocks are also similar to those for other ancient BIF and modern Si-Fe solid and fluid phases (fig. S7B; see the Supplementary Materials). We suggest that the similarities in REE + Y systematics of the NSB jasper-carbonate BIF with the NSB Fe-silicate BIF and other Archean jasper and BIF, as well as with some modern Si-Fe hydrothermal sediments, provide additional support for a primary seafloor origin. These data for the jasper-carbonate BIF are also inconsistent with a secondary formational process involving late postmetamorphic to recent Fe-rich oxidized fluids because such fluids would not produce positive Eu anomalies as these require deposition from high-temperature (>250°C) reduced fluids with predominance of the Eu²⁺ species over Eu³⁺ (52). Low normalized La/Yb ratios (<0.6; fig. S7G) are attributed to anomalous behavior of La in seawater and possibly also to syn- or postmetamorphic alteration by fluids depleted in light REE (53, 54).

Organic diagenesis and metamorphism

The metamorphically recrystallized, diagenetic origin of the nodules, granules, and rosettes in the NSB proposed here is supported by their association with relatively large (millimeter-size and substantially coarser than the matrix) recrystallized quartz, magnetite, hematite, calcite (Fig. 2A), apatite [Fig. 2B; (4)], and chalcocopyrite (Fig. 2, C and D). Such coarse crystals in chert are consistent with recrystallization of diagenetic precursor minerals. Inside the jasper nodules, millimeter-long blades of calcite have a texture of calcite + quartz rosettes containing micrometer-size inclusions of diagenetic (or metamorphic) apatite and quartz (Fig. 2, A and B). In BIF samples richer in carbonate, calcite rosettes also display a similar poikiloblastic texture and are typically cut by metamorphic stibnomelane (4). Calcite rosettes have concentric layers that contain micrometer-size graphitic carbon, as well as apatite crystals with sizes from a few micrometers up to about 1 mm (4). Recent studies have suggested that sedimentological structures with circularly concentric layers

and radially aligned crystals form during the abiotic decarboxylation of biomass from diagenetic decomposition (26, 27, 29). In the laboratory, chemically oscillating reactions produce similar patterns and have analogous compositions (malonic acid, bromate, bromide, sulfuric acid, and phenanthroline ferrous sulfate) to those reflected by the minerals present in rosettes, granules, and nodules from the NSB jasper-carbonate BIF (quartz + calcite-ankerite \pm magnetite/hematite \pm stilpnomelane \pm apatite \pm graphitic carbon). Hence, the outsized dimension and large size range of calcite and apatite crystals in the NSB carbonate-jasper BIF are also consistent with metamorphic recrystallization, whereas their poikilotopic textures, circularly concentric patterns, and mineral associations suggest the preservation of some diagenetically oxidized biomass.

Notably, microscopic inclusions of apatite and galena occur within outsized grains of chalcopyrite (Fig. 2E). This relationship is important because apatite in contact with galena occurring as inclusions in chalcopyrite is evidence of Pb-loss from apatite and S-diffusion from the host chalcopyrite during retrograde metamorphism. Apatite in the NSB jasper-carbonate BIF must therefore be originally syngenetic or diagenetic for Pb to have accumulated before peak metamorphism, which caused authigenic apatite to be open to Pb-loss, above 450°C (55), thus also implying that the age of this apatite is expected to reflect a metamorphic resetting. However, the micrometer-size galena in contact with apatite is also larger than expected from a source of Pb derived solely from the decay of U in apatite; therefore, some Pb likely also originated from a metalliferous chalcophilic environment, possibly related to seafloor-hydrothermal fluids. The host chalcopyrite contains myriad microscopic inclusions of galena, including some enriched in selenium (Fig. 2, F and G), further suggesting that the galena is likely authigenic within the chalcopyrite and metamorphic in origin. Hence, in our model, some Pb originated from chalcopyrite as well as from apatite inclusions, with the galena being attributed to a predominantly metamorphic origin, by which the galena-hosted Pb was originally in lattice substitutions in the chalcopyrite. This observation is relevant for the controversial origin of apatite within the Eoarchean quartz-pyroxene rock from Akilia in Greenland, which has a U-Pb age of 1504 ± 335 Ma (56), debated as possibly reset by thermal metamorphism (57). The Akilia apatite has been proposed as a biosignature due to its association with ^{13}C -depleted graphite (58, 59); thus, our notable observations of the NSB rocks contribute to the debate about young U-Pb ages in apatite from the Akilia quartz-pyroxene rock, claimed to be evidence for metamorphic crystallization of nonsyngenetic apatite (56, 60, 61). In summary, quartz, ferric-ferrous oxides, and apatite in the NSB jasper-carbonate BIF have a range of crystal sizes and occur in association with outsized calcite and chalcopyrite as well as with inclusions of graphitic carbon and galena. Such mineral assemblages are typical of fossils and biomass, and in this case are also consistent with expected products of the metamorphic recrystallization of a syngenetic, diagenetically oxidized, and hydrothermally influenced microbial community.

Primordial metal and sulfur pathways

Surface complexation modeling of trace metals (Mn, Co, Cu, Zn, Ni, Cd) in the NSB BIF is informative. This modeling has been used to predict the adsorption of such metals onto bacterial cells, a process that can lead to higher concentrations in BIF (62); therefore, enrichments of all of these specific elements in the jasper-carbonate BIF constitute another possible biosignature (Fig. 3A). However, in the absence of visually correlated concentrations of trace metals within

the hematite NSB pectinate-branching filaments, the observed high concentrations of these elements in the NSB jasper-carbonate BIF should be considered to only represent evidence of habitability and not necessarily microbial enrichments (Table 1). If the relatively high levels of vanadium and manganese are enriched also specifically in the microfossils described above, which is not yet known, the implication could then possibly relate to the biological concentration by nitrogen-fixing microorganisms, or to metabolic pathways that oxidize or reduce manganese.

In light of the unprecedented multiple sulfur isotope data presented here and empirical consideration that $\Delta^{33}\text{S}$ values well above $0.0 \pm 0.3\text{‰}$ can resolve a MIF signature, the NSB BIF samples have MIF signatures consistent with sedimentation under less than 0.0002% atmospheric oxygen (63). This signature is documented in chalcopyrite from the jasper-carbonate BIF, in pyrite and pyrrhotite from Fe-silicate BIF, and in pyrite from amphibolite, all of which are consistent with atmospheric sources of photolyzed sulfur aerosols in the sedimentary and volcanic rocks. Large ranges of markedly ^{34}S -enriched chalcopyrite in jasper are inconsistent with known abiotic fractionation in igneous systems, wherein $\delta^{34}\text{S}$ values of sulfide are less than $+5\text{‰}$ (64). Moreover, abiotic processes such as low-temperature hydrothermal fractionation (65) cannot easily explain the large ^{34}S -depletions and enrichments in the jasper, and abiotic processes such as Rayleigh fractionation during dehydration are also unlikely to cause the observed large range of positive $\delta^{34}\text{S}$ values. Microbial sulfate reduction under low sulfate concentrations is also considered unlikely because the oceanic sulfate concentration and its $\delta^{34}\text{S}_{\text{sulfate}}$ value in the NSB environment would have been close to zero molar and nearly 0‰ , respectively, and thus could not have produced the observed ^{34}S -enrichments. Instead, ^{34}S -enriched chalcopyrite in NSB jasper can be explained by microbially mediated elemental sulfur reduction or disproportionation of sulfite (SO_3). The former is known to be common in thermophilic bacteria and archaea and also is predicted to be the most ancient sulfur metabolic pathway (66); the latter can produce ^{34}S -enriched sulfate as high as $+12\text{‰}$ (67). However, ^{34}S -enrichments in chalcopyrite most commonly occur together with positive $\Delta^{33}\text{S}$ values (Fig. 4); hence, their MIF signatures imply that the sulfide is Archean in age and that the observed fractionation could reflect a mixing line between microbial sulfur disproportionation or sulfur reduction and abiotic photochemical reactions. Chalcopyrite from some jasper-carbonate BIF (PC0844) yields ^{34}S -enrichments as well as notable ^{33}S -enrichments. These positive isotopic enrichments are most likely sourced from S^0 aerosols rather than SO_4 (68). In summary, the lack of ^{34}S -enrichments elsewhere in the NSB (fig. S9) (23, 24) points to a localized phenomenon within the jasper-carbonate BIF, and thus possibly S-disproportionation in the original seafloor sediments, an interpretation that is also supported by the observations presented above regarding outcrops and petrographic textures and of the related microfossils and dubiofossils.

Broader implications

Field geologic relationships, micropaleontology, sedimentology, petrology, mineralogy, and geochemistry of the NSB jasper-carbonate BIF (Table 1) are all consistent with an original seafloor depositional environment, associated at an unknown distance from a basalt-hosted hydrothermal vent system. Preserved within this distinct rock are delicate primary structures, variably overprinted by diagenesis and metamorphism, that are interpretable as microfossils, dubiofossils, and abiotic biomorphs (Fig. 5). Given that abiotic

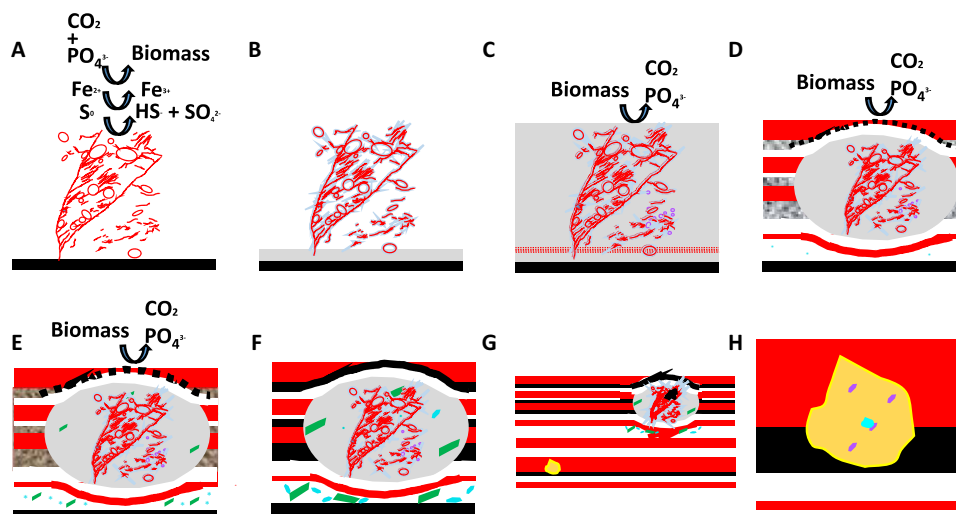


Fig. 5. Illustrative model for the inferred origin of microfossils in NSB jasper-carbonate BIF. (A) Metabolizing, organic-poor, pectinate-branching filaments of ferrihydrite with symbiotic colonies of irregular ellipsoids (red circles). (B) Postmortem colloidal silica (gray) precipitation on filaments and spheroids. (C) Ferrihydrite (red dots) coats the silica-permineralized filaments, forming parallel-aligned tubular structures, and onset of biomass oxidation in the siliceous ooze. (D) Early diagenetic nonequilibrium reactions of Liesegang diffusion of Fe-oxides form sedimentary layers, and chemically oscillating reactions during biomass oxidation produce jasper nodules and granules around microfossil colonies as well as hematite and carbonate rosettes (purple circles). (E) Decreased alkalinity during these reactions leads to quartz lithification and to the precipitation of micrometer-size carbonate (green), apatite (turquoise), hematite, and magnetite (black). (F and G) Prograde metamorphism leads to the formation of coarse-grained submillimeter carbonate, apatite, chalcopyrite (yellow), quartz, and magnetite (black), which blurs and partly deforms original textures and filaments. (H) Later retrograde metamorphism causes apatite to open and leak Pb, which forms galena in contact with apatite inside chalcopyrite, rendering U-Pb ages inconsistent with the age of the rock.

processes might explain certain features, and because of the notable postdepositional recrystallization suffered by the NSB jasper-carbonate BIF, some evidence for primordial microfossils remains ambiguous. However, higher preservation fidelity of the microfossils occurs in fine-grained quartz, likely due to the armoring effect of such micro-quartz as proposed for Phanerozoic seafloor-hydrothermal jaspers that preserve microbial filaments (69). Whereas the most recent geological map shows the jasper-carbonate BIF to occur along strike from the main stratabound Fe-silicate BIF unit, there is currently no detailed geological map available at high resolution that shows precise geological modes of occurrence. Obtaining this information would help to further demonstrate that the various observed micro-structures are not within younger cross-cutting veins or late box-work structures, as hypothesized by other workers without documented field evidence (15, 16). On the basis of available field and laboratory data, however, the jasper-carbonate BIF is suggested here to have originated as localized siliceous patches of ferric oxides and oxyhydroxides on the basaltic seafloor, like the settings reported for similar Fe-Si deposits on modern volcanic settings (44).

The mineralogical and sedimentological evidence for biosignatures in the NSB jasper-carbonate BIF includes millimeter-size crystals of calcite, apatite, chalcopyrite, quartz, and magnetite, all of which have a range of sizes consistent with the effects of metamorphic recrystallization on micrometer-size diagenetic precursors that formed during the oxidation of biomass. Variably recrystallized, undulated-to-coiled, hematite filaments in pectinate-branching structures are composed of mixed ferric-ferrous oxides and graphitic carbon, which together argue for the diagenetic reduction and metamorphic recrystallization of original organic-poor ferrihydrite filaments. If these filaments are considered dubiofossils and eventually are produced in abiotic

chemical gardens, the NSB specimens would still have important implications for prebiotic chemistry, such as an unforeseen prebiotic stage of evolution, and in the search for biosignatures on Mars and Europa. For instance, on Mars, millimeter-size early diagenetic hematite concretions occur in soils from Terra Meridiani (70) and in the Sheepbed Member of Gale Crater (71), both of which may contain biosignatures like those described here. A multiproxy approach and correlative microscopic analyses like those performed in this study might contribute critical information toward discovering a fossilized Early Martian biosphere.

Inferences here based on microfossil and dubiofossil morphology, stable isotope ratios of recrystallized diagenetic minerals, habitability of the depositional environment, and uniformitarian observations all point to several potential metabolic pathways for these primordial microbial communities. These pathways include Fe-oxidation and S-disproportionation, and possibly also anoxygenic photosynthesis. Implications for evolutionary biology are important and relate to the ancestry of the origin of life and of genes involved in bacterial S-disproportionation and Fe-oxidation. For the rock record, conclusions drawn from this work lend support to previous interpretations from Fe isotopes for microbial processes being involved in the origin of BIF, for an early rise of microaerophilic Fe-, S-, and C-metabolizing microbial communities, and for a number of biosignatures (Table 1) that can guide future studies of other Archean BIF. Moreover, the emerging model of abiotic diagenetic spheroids derived from chemically oscillating reactions can be applied to jasper-carbonate BIF and helps to comprehensively explain the occurrence of likely abiotic biomorphs such as rosettes, granules, and nodules in the NSB BIF, and the petrological context of microfossils contained within the granules and nodules. The NSB paleontological record demonstrates

that some minerals can effectively preserve biosignatures and microfossils in thermally recrystallized chemical-sedimentary rocks.

In summary, our unprecedented findings contribute to the search for extraterrestrial life by demonstrating that multiple co-occurring biosignatures (Table 1) including microfossils, dubiofossils, abiotic diagenetic microstructures, trace element compositions, and minerals associated with expected products from diagenetically oxidized biomass can yield a well-supported interpretation for early biological evolution. This discovery implies that only a few hundred million years are needed for life to evolve to an organized level on a primordial habitable planet. We therefore conclude that such microbial ecosystems could exist on other planetary surfaces where liquid water interacted with volcanic rocks, and that these oldest microfossils and dubiofossils reported here from the NSB suggest that extraterrestrial life may be more widespread than previously thought.

MATERIALS AND METHODS

Geological samples

Many geological samples analyzed in this work have been previously described elsewhere (4, 72). Representative images of field outcrops from which samples were collected are shown in fig. S1, in the context of the associated metavolcanic rocks. Samples PC0822 (N58°16'50.9"; W77°44'14.7"), PC0823 (N58°16'50.9"; W77°44'14.7"), PC0824 (N58°16'50.9"; W77°44'14.7"), PC0828 (N58°17'09.1"; W77°44'10.8"), and PC0844 (N58°16'53.8"; W77°44'14.1") are jasper-carbonate BIF, all of which were collected from stratabound outcrops located along strike and within the main linear BIF unit of the NSB. Samples PC0802 (N58°16'43.5"; W77°43'57.7"), PC0804 (N58°17'49.8"; W77°44'04.9"), PC0814 (N58°17'12.3"; W77°44'11.6"), PC0815 (N58°17'12.3"; W77°44'11.6"), PC0830 (N58°16'56.5"; W77°43'28.3"), PC0838 (N58°16'45.3"; W77°43'54.1"), and PC0848 (N58°17'41.3"; W77°44'03.3") are all Fe-silicate BIF variably dominated by quartz, magnetite, and cummingtonite-grunerite and also come from stratabound zones located along strike and within the main linear BIF unit of the NSB. Samples PC0829 (N58°16'56.5"; W77°43'28.3"), PC0836 (N58°16'45.3"; W77°43'54.1"), and PC0846 (N58°16'43.2"; W77°43'58.5") are all cummingtonite-garnet amphibolites occurring either within or adjacent to Fe-silicate BIF.

Optical microscopy and bulk geochemical analyses

Optical microscopy was performed with a BX-51 Olympus microscope at University College London (UCL) equipped with reflected and transmitted light and with the following objectives: 5×, 10×, 20×, 50×, and 100×. No oil immersion or ink markings were used on the thin and thick sections. Cross-polar images were acquired on 30- and 60- μm -thick thin sections: Coarse quartz has first-order yellow to second-order purple interference colors in thicker thin sections. Microscopic irregular ellipsoids were measured using the Stream Start 1.9 software provided by Olympus. Two measurements were used to calculate the average size of the irregular ellipsoids with the long and short lengths as well as to calculate the aspect ratio (long length divided by short length). For the diameter of pectinate-branching filaments, three measurements along each length were averaged (only those with lengths more than ca. 200 μm were considered for this analysis).

Bulk geochemical analyses were conducted in the Laboratory of Environmental Geochemistry (LEGS) at the University of Colorado

at Boulder using an inductively coupled plasma-atomic emission spectroscopy (ICP-AES) and an ICP-MS. Analyses of standards and selected duplicate analyses are shown in table S1 and yield an accuracy better than 1% for major elements, 0.1 ppm for minor and trace elements, and better than 5 ppb (parts per billion) for REE.

Micro-Raman and scanning electron microscopy

Micro-Raman was performed primarily with the α 300 WITec confocal laser scanning microspectroscopy system at UCL, using a laser tuned to between 7 and 12 mW, following previously described techniques (27, 72). The WITec α 300 Raman system was used to image carbonate + apatite + stilpnomelane + magnetite rosettes in PC0844 and PC0822. The WITec-Tescan RISE Raman-SEM (scanning electron microscopy) system at China University of Geosciences (CUG) was used to obtain visually correlated, low-resolution Raman-SEM images of oversized calcite crystals and hematite rosettes in the polished slab of PC0822, whereas the JEOL 6500F field-emission SEM at the Geophysical Laboratory of the Carnegie Institution for Science was used to image sulfide crystals.

Focused ion beam nanofabrication

Analyses by focused ion beam (FIB) were done at the London Centre for Nanotechnology, with a Zeiss NV40 dual beam FIB-SEM instrument. This work was performed with the goal of creating a three-dimensional (3D) tomographic reconstruction of an undulated hematite filament. A total of 160 slices of 400 nm in thickness were nanofabricated by FIB and photographed using BSE imaging. A primary Ga beam of 13 nA at 30 keV was used on the gold-coated polished thin section. The stage was inclined at 36°, and a corresponding tilt correction was used for BSE imaging (voltage potential = 1.50 kV). Operating vacuum was ca. 7.5×10^{-7} mbar, and the magnification was manually kept at $\times 4000$. Exposure time for BSE images was set at speed 6 in the Zeiss control software (about 60 s), which took about 5 min per slice. This process was repeated manually to ensure that pillars formed during milling (e.g., due to material of variable milling rates) were completely removed. The 3D visual reconstruction of the undulated filament is performed using the following approach: Images were aligned according to the top linear feature marking the cut or milled corner of quartz with the gold coat. The images were then serially stacked and segmented, and a video was created using Avizo 9.0 software.

Micro-computed tomography

Micro-computed tomography (CT) analysis was performed using the Zeiss Xradia 520 Versa platform at UCL that uses an optically coupled, two-stage magnification system. A columnar, square-shaped sample of about 5 mm on each side and 3.5 cm high was cut from a slab through the PC0822 nodule and has its sides polished. During imaging, a total of 1201 radiographs were acquired over a 360° sample rotation range with an exposure time of 3 s per radiograph. The samples are placed between the x-ray source and a $2\text{k} \times 2\text{k}$ detector; a source-to-detector distance of 38.75 mm provided a voxel resolution of 1.10 μm using the 4× objective magnification in binning 1 mode. The instrument was operated at 110 kV and 91 μA , without any filter in place. Raw transmission images from microscale CT imaging experiments were reconstructed using a commercial image reconstruction software package (Zeiss XMReconstructor, Carl Zeiss X-ray Microscopy Inc., Pleasanton, CA), which uses a filtered back-projection algorithm. The reconstructed grayscale 3D image volumes were subsequently

segmented using the Avizo software package (Avizo 9.0, Thermo Fisher Scientific, Waltham, MA, USA). Details of the experimental conditions are as follows: Number of projections was 1201, voltage potential was 110 kV, current was 91 μ A, exposure time was 3 s, pixel size was 1.10, binning acquisition was 1, binning reconstruction was 1, optical magnification was $\times 4$, field of view was 2250 μ m, and sample Y position was -2220.60μ m.

Multiple sulfur isotope of sulfide minerals by NanoSIMS

These analyses were performed using NanoSIMS 50L located at the Carnegie Institution of Science (Washington, DC, USA), for which the method is described in detail in (21), hence is only summarized briefly here. Slabs were manually made into 1-cm-diameter disks and polished down to 250-nm Al_2O_3 . The slabs are cleaned with deionized (DI) water and then with acetone and subsequently coated with gold and kept under vacuum at 10^{-4} mbar in an oven at 50°C or 10^{-6} mbar in the carousel of the NanoSIMS. Standards were mounted in the same eight-sample “Biologie” holder and consist of gold-coated, acetone + DI water-cleaned, polished, and indium-pressed sulfide standards that include Balmat pyrite, Anderson pyrrhotite, and Trout Lake chalcopyrite (24, 73–75). Because all samples were coated with a few nanometers of gold, a presputtering of 180 s was used on the surface with the Cs beam, with the following NanoSIMS-specific (CAMECA 50L) settings: the FCp detector downstream of the Cs source after the L0-L2 lenses measured 26.92 nA of beam current with D0-0 and the FCo detector at the sample stage position measured 1.48 nA, with D1-2 used for all analyses. The focused Cs beam was rastered over a $15 \mu\text{m} \times 15 \mu\text{m}$ spot for 10 blocks of 40 cycles each for a combined analysis time of about 12.5 min per spot. An electron beam was used for charge compensation at the sample surface and is set with a constant LF6 and LF7. Baseline correction was done by measuring the baseline four times before and during each analysis. LF2 and Cy were manually optimized for every spot to ensure a consistent and stable secondary ion count. Exit slits at the detector were ExS4-1, ExS5-2, and ExS6-2, and each of the respective electrostatic analyzer was tuned to optimize count rates. Other slits used include ES-4, AS-3, and EnS-0. The mass resolving power was set at 8300, and the magnetic field was stabilized with an autoregulated nuclear magnetic resonance. The data shown in table S3A are for NSB sulfides, whereas table S3B presents analyses on standards corrected for “instrumental mass fractionation” for each respective sulfide phase; the $\Delta^{33}\text{S}$ values and associated errors are calculated via a York-based regression using a previously described approach (75).

Multiple sulfur isotope analyses by the continuous flow - elemental analysis - isotope ratio mass spectrometry sulfur oxide (CF-EA-IRMS SO) method

The sulfide standard and microdrilled samples were accurately weighed to the nearest microgram into small tin boats, and tests are done with and without added V_2O_5 granules, representing about one-third the weight of the standard/sample sulfide powder when added. The packed boats were then placed in the carousel to be dropped in the oxidizing reactor filled with tungstic oxide and copper wire. Tests done on results obtained with and without blanks in the carousel or V_2O_5 in the tin boat lack statistically significant differences (table S4B). The standards and samples were then combusted in the reactor of a Carlo Erba NC2100 elemental analyzer fitted with a gas chromatographic column of 20 cm in length and no water trap. The $\text{SO}-\text{SO}_2$ gas mixture was transferred directly to the inlet of the Delta

V isotope-ratio mass spectrometer at Boston College (Chestnut Hill, MA, USA); ions were detected simultaneously by the six collector Faraday cup system (22). Results for micro-drillates are shown in table S4A; analyses of sulfide standards analyzed during the session are listed in table S4B. Results on standard Cañon Diablo troilite show a 1σ deviation of 0.26‰ for $\delta^{34}\text{S}$ and of 0.18‰ for $\delta^{33}\text{S}$, with calculations performed using the SO method of Baubly *et al.* (22). $\Delta^{33}\text{S}$ values are calculated by the equation: $\Delta^{33}\text{S} = \delta^{33}\text{S} - 1000 \times (1 + \delta^{34}\text{S}/1000)^{0.515} - 1$, and analyses of CDT show a $\delta^{33}\text{S}$ 1σ SD of 0.13‰ that is well below the conservatively estimated ± 0.30 ‰ MDF band plotted in Fig. 4B, as calculated using the York-based regression technique. Considering the statistical significance of the dataset of standards analyzed between the samples in each technique (fig. S9B and table S3B) and the largely overlapping range of $\delta^{34}\text{S}$ and $\Delta^{33}\text{S}$ values for chalcopyrite, pyrite, and pyrrhotite from both techniques (fig. S9 and table S5), it can be concluded that these overlapping ranges of multiple sulfur isotope values from the two analytical techniques represent excellent internal consistency.

SUPPLEMENTARY MATERIALS

Supplementary material for this article is available at <https://science.org/doi/10.1126/sciadv.abm2296>

REFERENCES AND NOTES

1. A. Kappler, C. Pasquero, K. O. Konhauser, D. K. Newman, Deposition of banded iron formations by anoxygenic phototrophic Fe(II)-oxidizing bacteria. *Geology* **33**, 865 (2005).
2. A. D. Czaja, C. M. Johnson, B. L. Beard, E. E. Roden, L. Weiqiang, S. Moorbath, Biological Fe oxidation controlled deposition of banded iron formation in the ca. 3770Ma Isua Supracrustal Belt (West Greenland). *Earth Planet. Sci. Lett.* **363**, 192–203 (2013).
3. N. Dauphas, N. L. Cates, S. J. Mojzsis, V. Busigny, Identification of chemical sedimentary protoliths using iron isotopes in the >3750 Ma Nuvvuagittuq supracrustal belt, Canada. *Earth Planet. Sci. Lett.* **254**, 358–376 (2007).
4. M. S. Dodd, D. Papineau, T. Grenne, J. F. Slack, M. Rittner, F. Pirajno, J. O’Neil, C. T. S. Little, Evidence for early life in Earth’s oldest hydrothermal vent precipitates. *Nature* **543**, 60–64 (2017).
5. N. L. Cates, S. J. Mojzsis, Pre-3750 Ma supracrustal rocks from the Nuvvuagittuq supracrustal belt, northern Québec. *Earth Planet. Sci. Lett.* **255**, 9–21 (2007).
6. J. O’Neil, C. Maurice, R. K. Stevenson, J. Larocque, C. Cloquet, J. David, and D. Francis, The geology of the 3.8 Ga Nuvvuagittuq (Porpoise Cove) Greenstone Belt, Northeastern Superior Province, Canada, in *Earth’s Oldest Rocks*, M. J. v. Kranendonk, R. H. Smithies, V. C. Bennett, Eds. (Elsevier B.V, 2007), vol. 15, pp. 219–250.
7. J. M. Garcia-Ruiz, E. Melero-Garcia, S. T. Hyde, Morphogenesis of self-assembled nanocrystalline materials of barium carbonate and silica. *Science* **323**, 362–365 (2009).
8. J. M. Garcia-Ruiz, S. T. Hyde, A. M. Carnerup, A. G. Christy, M. J. Van Kranendonk, N. J. Welham, Self-assembled silica-carbonate structures and detection of ancient microfossils. *Science* **302**, 1194–1197 (2003).
9. J. M. Garcia-Ruiz, E. Nakouzi, E. Kotopoulou, L. Tamborrino, O. Steinbock, Biomimetic mineral self-organization from silica-rich spring waters. *Sci. Adv.* **3**, 160–170 (2017).
10. L. M. Barge, S. S. S. Cardoso, J. H. E. Cartwright, G. J. T. Cooper, L. Cronin, A. de Wit, I. J. Doloboff, B. Escribano, R. E. Goldstein, F. Haudin, D. E. H. Jones, A. L. Mackay, J. Maseiko, J. J. Pagano, J. Pantaleone, M. J. Russell, C. I. Sainz-Diaz, O. Steinbock, D. A. Stone, Y. Tanimoto, N. L. Thomas, From chemical gardens to chemobionics. *Chem. Rev.* **115**, 8652–8703 (2015).
11. E. Nakouzi, O. Steinbock, Self-organization in precipitation reactions far from the equilibrium. *Sci. Adv.* **2**, e1601144 (2016).
12. K. C. Johannessen, N. McLoughlin, P. E. Vullum, I. H. Thorseth, On the biogenicity of Fe-oxhydroxide filaments in silicified low-temperature hydrothermal deposits: Implications for the identification of Fe-oxidizing bacteria in the rock record. *Geobiology* **18**, 31–53 (2020).
13. S. McMahon, Earth’s earliest and deepest purported fossils may be iron-mineralized chemical gardens. *Proc. R. Soc. B Biol. Sci.* **286**, 20192410 (2019).
14. J. O’Neil, D. Francis, R. W. Carlson, Implications of the Nuvvuagittuq greenstone belt for the formation of Earth’s early crust. *J. Petrol.* **52**, 985–1009 (2011).
15. W. Chowdhury, D. Trail, M. Guitreau, E. A. Bell, J. Buettner, S. J. Mojzsis, Geochemical and textural investigations of the Eoarchean Ukaliq supracrustals, Northern Québec (Canada). *Lithos* **372–373**, 105673 (2020).

16. J. Greer, G. Caro, N. L. Cates, P. Tropper, W. Bleeker, N. M. Kelly, S. J. Mojzsis, Widespread poly-metamorphosed Archean granitoid gneisses and supracrustal enclaves of the southern Inukjuak Domain, Québec (Canada). *Lithos* **364–365**, 105520 (2020).
17. H. F. J. Theart, R. Ghavami-Riabi, H. Mouri, P. Gräser, Applying the box plot to the recognition of footwall alteration zones related to VMS deposits in a high-grade metamorphic terrain, South Africa, a litho-geochemical exploration application. *Geochemistry* **71**, 143–154 (2011).
18. A. Picard, A. Kappler, G. Schmid, L. Quaroni, M. Obst, Experimental diagenesis of organo-mineral structures formed by microaerophilic Fe(II)-oxidizing bacteria. *Nat. Commun.* **6**, 6277 (2015).
19. G. L. Laberge, Possible biological origin of precambrian iron-formations. *Econ. Geol.* **68**, 1098–1109 (1973).
20. T. Grenne, J. F. Slack, Paleozoic and Mesozoic silica-rich seawater: Evidence from hematitic chert (jasper) deposits. *Geology* **31**, 319–322 (2003).
21. E. H. Hauri, D. Papineau, J. Wang, F. Hillion, High-precision analysis of multiple sulfur isotopes using NanoSIMS. *Chem. Geol.* **420**, 148–161 (2016).
22. K. A. Baublys, S. D. Golding, E. Young, B. S. Kamber, Simultaneous determination of $\delta^{33}\text{S}$ -CDT and $\delta^{34}\text{S}$ -CDT using masses 48, 49 and 50 on a continuous flow isotope ratio mass spectrometer. *Rapid Commun. Mass Spectrom.* **18**, 2765–2769 (2004).
23. E. Thomassot, J. O'Neil, D. Francis, P. Cartigny, B. A. Wing, Atmospheric record in the Hadean Eon from multiple sulfur isotope measurements in Nuvvuagittuq Greenstone Belt (Nunavik, Quebec). *Proc. Natl. Acad. Sci. U.S.A.* **112**, 707–712 (2015).
24. N. L. Cates, K. Ziegler, A. K. Schmitt, S. J. Mojzsis, Reduced, reused and recycled: Detrital zircons define a maximum age for the Eoarchean (ca. 3750–3780Ma) Nuvvuagittuq Supracrustal Belt, Québec (Canada). *Earth Planet. Sci. Lett.* **362**, 283–293 (2013).
25. M. S. Dodd, D. Papineau, Z. She, M. L. Fogel, S. Nederbragt, F. Pirajno, Organic remains in late Palaeoproterozoic granular iron formations and implications for the origin of granules. *Precambrian Res.* **310**, 133–152 (2018).
26. D. Papineau, Z. She, M. S. Dodd, Chemically-oscillating reactions during the diagenetic oxidation of organic matter and in the formation of granules in late Palaeoproterozoic chert from Lake Superior. *Chem. Geol.* **470**, 33–54 (2017).
27. D. Papineau, B. de Gregorio, S. Fearn, D. Kilcoyne, G. McMahon, R. Purohit, M. Fogel, Nanoscale petrographic and geochemical insights on the origin of the Palaeoproterozoic stromatolitic phosphorites from Aravalli Supergroup, India. *Geobiology* **14**, 3–32 (2016).
28. A. N. Zaikin, A. M. Zhabotinsky, Concentration wave propagation in two-dimensional liquid-phase self-oscillating system. *Nature* **225**, 535–537 (1970).
29. D. Papineau, J. Yin, K. G. Devine, D. Liu, Z. She, Chemically oscillating reactions during the diagenetic formation of ediacaran siliceous and carbonate botryoids. *Minerals* **11**, 1060 (2021).
30. L. M. Barge, I. J. Doloboff, L. M. White, G. D. Stucky, M. J. Russell, I. Kanik, Characterization of iron-phosphate-silicate chemical garden structures. *Langmuir* **28**, 3714–3721 (2012).
31. M. J. Russell, L. M. Barge, R. Bhartia, D. Bocanegra, P. J. Bracher, E. Branscomb, R. Kidd, S. McGlynn, D. H. Meier, W. Nitschke, T. Shibuya, S. Vance, L. White, I. Kanik, The drive to life on wet and icy worlds. *Astrobiology* **14**, 308–343 (2014).
32. J. M. Garclá-Ruiz, Inorganic self-organisation in precambrian cherts. *Orig. Life Evol. Biosph.* **24**, 451–467 (1994).
33. S. F. Jordan, H. Ramm, I. N. Zheludev, A. M. Hartley, A. Maréchal, N. Lane, Promotion of protocell self-assembly from mixed amphiphiles at the origin of life. *Nat. Ecol. Evol.* **3**, 1705–1714 (2019).
34. C. Nims, J. Lafond, J. Alleon, A. S. Templeton, J. Cosmidis, Organic biomorphs may be better preserved than microorganisms in early Earth sediments. *Geology* **49**, 629–634 (2021).
35. J. H. E. Cartwright, B. Escribano, C. I. Sainz-Díaz, L. S. Stodieck, Chemical-Garden formation, morphology, and composition. II. Chemical gardens in microgravity. *Langmuir* **27**, 3294–3300 (2011).
36. J. Götz, *Mineralogy of Quartz and Silica Minerals* (MDPI Books, 2018), 274 pp.
37. J. Rouillard, J. M. García-Ruiz, L. Kah, E. Gérard, L. Barrier, S. Nabhan, J. Gong, M. A. Zuilen, Identifying microbial life in rocks: Insights from population morphometry. *Geobiology* **18**, 282–305 (2020).
38. D. Liu, N. Yu, D. Papineau, Q. Fan, H. Wang, X. Qiu, Z. She, G. Luo, The catalytic role of planktonic aerobic heterotrophic bacteria in protodolomite formation: Results from Lake Jibuhulangtu Nur, Inner Mongolia, China. *Geochim. Cosmochim. Acta* **263**, 31–49 (2019).
39. D. Papineau, Chemically oscillating reactions in the formation of botryoidal malachite. *Am. Mineral.* **105**, 447–454 (2020).
40. D. Deamer, B. Damer, V. Kompanichenko, Hydrothermal chemistry and the origin of cellular life. *Astrobiology* **19**, 1523–1537 (2019).
41. C. T. S. Little, S. E. J. Glynn, R. A. Mills, Four-hundred-and-ninety-million-year record of bacteriogenic iron oxide precipitation at sea-floor hydrothermal vents. *Geomicrobiol. J.* **21**, 415–429 (2004).
42. D. Emerson, C. L. Moyer, Neutrophilic Fe-oxidizing bacteria are abundant at the Loihi Seamount hydrothermal vents and play a major role in Fe oxide deposition. *Appl. Environ. Microbiol.* **68**, 3085–3093 (2002).
43. T. D. Boyd, S. D. Scott, Microbial and hydrothermal aspects of ferric oxyhydroxides and ferrous hydroxides: The example of Franklin Seamount, Western Woodlark Basin, Papua New Guinea. *Geochem. Trans.* **2**, 2–45 (2001).
44. K. J. Edwards, B. T. Glazer, O. J. Rouxel, W. Bach, D. Emerson, R. E. Davis, B. M. Toner, C. S. Chan, B. M. Tebo, H. Staudigel, C. L. Moyer, Ultra-diffuse hydrothermal venting supports Fe-oxidizing bacteria and massive amber deposition at 5000 m off Hawaii. *ISME J.* **5**, 1748–1758 (2011).
45. X. Peng, H. Zhou, J. Li, J. Li, S. Chen, H. Yao, Z. Wu, Intracellular and extracellular mineralization of a microbial community in the Edmond deep-sea vent field environment. *Sediment. Geol.* **229**, 193–206 (2010).
46. G. Proskurowski, M. D. Lilley, J. S. Seewald, G. L. Früh-Green, E. J. Olson, J. E. Lupton, S. P. Sylva, D. S. Kelley, Abiogenic hydrocarbon production at Lost City hydrothermal field. *Science* **319**, 604–607 (2008).
47. D. Wacey, M. R. Kilburn, M. Saunders, J. Cliff, M. D. Brasier, Microfossils of sulphur-metabolizing cells in 3.4-billion-year-old rocks of Western Australia. *Nat. Geosci.* **4**, 698–702 (2011).
48. M. Homann, Earliest life on Earth: Evidence from the Barberton Greenstone Belt, South Africa. *Earth Sci. Rev.* **196**, 102888 (2019).
49. R. S. Shapiro, K. O. Konhauser, Hematite-coated microfossils: Primary ecological fingerprint or taphonomic oddity of the Paleoproterozoic? *Geobiology* **13**, 209–224 (2015).
50. J. W. Schopf, A. B. Kudryavtsev, Confocal laser scanning microscopy and Raman imagery of ancient microscopic fossils. *Precambrian Res.* **173**, 39–49 (2009).
51. J. T. Beatty, J. Overmann, M. T. Lince, A. K. Manske, A. S. Lang, R. E. Blankenship, C. L. van Dover, T. A. Martinson, F. G. Plumley, An obligately photosynthetic bacterial anaerobe from a deep-sea hydrothermal vent. *Proc. Natl. Acad. Sci. U.S.A.* **102**, 9306–9310 (2005).
52. M. Bau, Rare-earth element mobility during hydrothermal and metamorphic fluid-rock interaction and the significance of the oxidation state of europium. *Chem. Geol.* **93**, 219–230 (1991).
53. R. Bolhar, M. J. Van Kranendonk, B. S. Kamber, A trace element study of siderite–jasper banded iron formation in the 3.45Ga Warrawoona Group, Pilbara Craton—Formation from hydrothermal fluids and shallow seawater. *Precambrian Res.* **137**, 93–114 (2005).
54. P. Bonnand, S. V. Lalonde, M. Boyet, C. Heubeck, M. Homann, P. Nonnotte, I. Foster, K. O. Konhauser, I. Köhler, Post-depositional REE mobility in a Paleoproterozoic banded iron formation revealed by La-Ce geochronology: A cautionary tale for signals of ancient oxygenation. *Earth Planet. Sci. Lett.* **547**, 116452 (2020).
55. D. J. Cherniak, W. A. Lanford, F. J. Ryerson, Lead diffusion in apatite and zircon using ion implantation and Rutherford Backscattering techniques. *Geochim. Cosmochim. Acta* **55**, 1663–1673 (1991).
56. Y. Sano, K. Terada, Y. Takahashi, A. P. Nutman, Origin of life from apatite dating? *Nature* **400**, 127–128 (1999).
57. J. M. Eiler, The oldest fossil or just another rock? *Science* **317**, 1046–1047 (2007).
58. S. J. Mojzsis, G. Arrhenius, K. D. McKeegan, T. M. Harrison, A. P. Nutman, C. R. L. Friend, Evidence for life on Earth before 3,800 million years ago. *Nature* **384**, 55–59 (1996).
59. K. D. McKeegan, A. B. Kudryavtsev, J. W. Schopf, Raman and ion microscopic imagery of graphitic inclusions in apatite from older than 3830 Ma Akilia supracrustal rocks, west Greenland. *Geology* **35**, 591–594 (2007).
60. A. Lepland, M. A. van Zuilen, P. Philippot, Fluid-deposited graphite and its geobiological implications in early Archean gneiss from Akilia, Greenland. *Geobiology* **9**, 2–9 (2011).
61. S. Moorbath, Dating earliest life. *Nature* **434**, 155 (2005).
62. R. E. Martinez, K. O. Konhauser, N. Paunova, W. Wu, D. S. Alessi, A. Kappler, Surface reactivity of the anaerobic phototrophic Fe(II)-oxidizing bacterium *Rhodovulum iodolum*: Implications for trace metal budgets in ancient oceans and banded iron formations. *Chem. Geol.* **442**, 113–120 (2016).
63. A. A. Pavlov, J. F. Kasting, Mass-independent fractionation of sulfur isotopes in Archean sediments: Strong evidence for an anoxic Archean atmosphere. *Astrobiology* **2**, 27–41 (2002).
64. R. O. Rye, A review of the stable-isotope geochemistry of sulfate minerals in selected igneous environments and related hydrothermal systems. *Chem. Geol.* **215**, 5–36 (2005).
65. H. Ohmoto, M. B. Goldhaber, Geochemistry of hydrothermal ore deposits, in *Geochemistry of Hydrothermal Ore Deposits*, H. L. Barnes, Ed. (Wiley, ed. 3, 1997).
66. D. E. Canfield, R. Raiswell, The evolution of the sulfur cycle. *Am. J. Sci.* **299**, 697–723 (1999).
67. K. S. Habicht, D. E. Canfield, J. Rethmeier, Sulfur isotope fractionation during bacterial reduction and disproportionation of thiosulfate and sulfite. *Geochim. Cosmochim. Acta* **62**, 2585–2595 (1998).
68. J. Farquhar, B. Huming, M. Thieme, Atmospheric influence of Earth's earliest sulfur cycle. *Science* **289**, 756–758 (2000).
69. N. C. Duhig, J. Stolz, G. J. Davidson, R. R. Large, Cambrian microbial and silica gel textures in silica iron exhalites from the Mount Windsor volcanic belt, Australia; their petrography, chemistry, and origin. *Econ. Geol. Bull. Soc. Econ. Geol.* **87**, 764–784 (1992).

70. S. W. Squyres, R. E. Arvidson, Bell JF 3rd, J. Brückner, N. A. Cabrol, W. Calvin, M. H. Carr, P. R. Christensen, B. C. Clark, L. Crumpler, D. J. Marais, C. d'Uston, T. Economou, J. Farmer, W. Farrand, W. Folkner, M. Golombek, S. Gorevan, J. A. Grant, R. Greeley, J. Grotzinger, L. Haskin, K. E. Herkenhoff, S. Hviid, J. Johnson, G. Klingelhöfer, A. H. Knoll, G. Landis, M. Lemmon, R. Li, M. B. Madsen, M. C. Malin, S. McLennan, H. McSween, D. W. Ming, J. Moersch, R. V. Morris, T. Parker, Rice JW Jr, L. Richter, R. Rieder, M. Sims, M. Smith, P. Smith, A. M. Soderblom, R. Sullivan, H. Wänke, T. Wdowiak, M. Wolff, A. Yen, The Opportunity Rover's Athena Science Investigation at Meridiani Planum, Mars. *Science* **306**, 1698–1703 (2004).
71. S. M. McLennan, R. B. Anderson, J. F. Bell III, J. C. Bridges, F. Calef III, J. L. Campbell, B. C. Clark, S. Clegg, P. Conrad, A. Cousin, D. J. D. Marais, G. Dromart, M. D. Dyar, L. A. Edgar, B. L. Ehlmann, C. Fabre, O. Forni, O. Gasnault, R. Gellert, S. Gordon, J. A. Grant, J. P. Grotzinger, S. Gupta, K. E. Herkenhoff, J. A. Hurovitz, P. L. King, S. Le Mouélic, L. A. Leshin, R. Léveillé, K. W. Lewis, N. Mangold, S. Maurice, D. W. Ming, R. V. Morris, M. Nachon, H. E. Newsom, A. M. Ollila, G. M. Perrett, M. S. Rice, M. E. Schmidt, S. P. Schwenzer, K. Stack, E. M. Stolper, D. Y. Sumner, A. H. Treiman, S. Van Bommel, D. T. Vaniman, A. Vasavada, R. C. Wiens, R. A. Yingst; MSL Science Team, Elemental geochemistry of sedimentary rocks at Yellowknife Bay, Gale Crater, Mars. *Science* **343**, 1244734 (2014).
72. D. Papineau, B. T. De Gregorio, G. D. Cody, J. O'Neil, A. Steele, R. M. Stroud, M. L. Fogel, Young poorly crystalline graphite in the >3.8-Gyr-old Nuvvuagittuq banded iron formation. *Nat. Geosci.* **4**, 376–379 (2011).
73. S. J. Mojzsis, C. D. Coath, J. P. Greenwood, K. D. McKeegan, T. M. Harrison, Mass-independent isotope effects in Archean (2.5 to 3.8 Ga) sedimentary sulfides determined by ion microprobe analysis. *Geochim. Cosmochim. Acta* **67**, 1635–1658 (2003).
74. D. Papineau, S. J. Mojzsis, C. D. Coath, J. A. Karhu, K. D. McKeegan, Multiple sulfur isotopes of sulfides from sediments in the aftermath of Paleoproterozoic glaciations. *Geochim. Cosmochim. Acta* **69**, 5033–5060 (2005).
75. D. Papineau, S. J. Mojzsis, A. K. Schmitt, Multiple sulfur isotopes from Paleoproterozoic Huronian interglacial sediments and the rise of atmospheric oxygen. *Earth Planet. Sci. Lett.* **255**, 188–212 (2007).
76. D. S. Alibo, Y. Nozaki, Rare earth elements in seawater: Particle association, shale-normalization, and Ce oxidation. *Geochim. Cosmochim. Acta* **63**, 363–372 (1999).
77. M. Bau, P. Dulski, Comparing yttrium and rare earths in hydrothermal fluids from the Mid-Atlantic Ridge: Implications for Y and REE behaviour during near-vent mixing and for the Y/Ho ratio of Proterozoic seawater. *Chem. Geol.* **155**, 77–90 (1999).
78. M. Bau, P. Dulski, Distribution of yttrium and rare-earth elements in the Penge and Kuruman iron-formations, Transvaal Supergroup, South Africa. *Precambrian Res.* **79**, 37–55 (1996).
79. C. S. Chan, S. C. Fakra, D. Emerson, E. J. Fleming, K. J. Edwards, Lithotrophic iron-oxidizing bacteria produce organic stalks to control mineral growth: Implications for biosignature formation. *ISME J.* **5**, 717–727 (2011).
80. C. S. Chan, S. M. McAllister, A. H. Leavitt, B. T. Glazer, S. T. Krepeski, D. Emerson, The architecture of iron microbial mats reflects the adaptation of chemolithotrophic iron oxidation in freshwater and marine environments. *Front. Microbiol.* **7**, 796 (2016).
81. E. Douville, P. Bienvenu, J. L. Charlou, J. P. Donval, Y. Fouquet, P. Appriou, T. Gamo, Yttrium and rare earth elements in fluids from various deep-sea hydrothermal systems. *Geochim. Cosmochim. Acta* **63**, 627–643 (1999).
82. H. N. Edmonds, C. R. German, Particle geochemistry in the Rainbow hydrothermal plume, Mid-Atlantic Ridge. *Geochim. Cosmochim. Acta* **68**, 759–772 (2004).
83. A. Ehrenreich, F. Widdel, Anaerobic oxidation of ferrous iron by purple bacteria, a new type of phototrophic metabolism. *Appl. Environ. Microbiol.* **60**, 4517–4526 (1994).
84. R. Frei, A. Polat, Source heterogeneity for the major components of ~3.7 Ga Banded Iron Formations (Isua Greenstone Belt, Western Greenland): Tracing the nature of interacting water masses in BIF formation. *Earth Planet. Sci. Lett.* **253**, 266–281 (2007).
85. B. Gourcerol, P. C. Thurston, D. J. Kontak, O. Côté-Mantha, J. Biczok, Depositional setting of Algoma-type banded iron formation. *Precambrian Res.* **281**, 47–79 (2016).
86. B. A. Haley, G. P. Klinkhammer, J. McManus, Rare earth elements in pore waters of marine sediments. *Geochim. Cosmochim. Acta* **68**, 1265–1279 (2004).
87. J. R. Hein, D. A. Clague, R. A. Koski, R. W. Embley, R. E. Dunham, Metalliferous sediment and a silica-hematite deposit within the Blanco fracture zone, Northeast Pacific. *Mar. Georesour. Geotechnol.* **26**, 317–339 (2008).
88. K. C. Johannessen, J. Vander Roost, H. Dahle, S. H. Dundas, R. B. Pedersen, I. H. Thorseth, Environmental controls on biomineralization and Fe-mound formation in a low-temperature hydrothermal system at the Jan Mayen Vent Fields. *Geochim. Cosmochim. Acta* **202**, 101–123 (2017).
89. G. Y. Jung, H. O. Jung, J. R. Kim, Y. Ahn, S. Park, Isolation and characterization of *Rhodospseudomonas palustris* P4 which utilizes CO with the production of H₂. *Biotechnol. Lett.* **21**, 525–529 (1999).
90. S. Liao, C. Tao, H. Li, G. Zhang, J. Liang, W. Yang, Y. Wang, Surface sediment geochemistry and hydrothermal activity indicators in the Dragon Horn area on the Southwest Indian Ridge. *Mar. Geol.* **398**, 22–34 (2018).
91. C. T. S. Little, K. C. Johannessen, S. Bengtson, C. S. Chan, M. Ivarsson, J. F. Slack, C. Broman, I. H. Thorseth, T. Grenne, O. J. Rouxel, A. Bekker, A late Paleoproterozoic (1.74 Ga) deep-sea, low-temperature, iron-oxidizing microbial hydrothermal vent community from Arizona, USA. *Geobiology* **19**, 228–249 (2021).
92. S. M. Luedin, N. Liechti, R. P. Cox, F. Danza, N. U. Frigaard, N. R. Posth, J. F. Pothier, S. Roman, N. Storelli, M. Wittwer, M. Tonolla, Draft genome sequence of chromatium okenii isolated from the stratified alpine lake cadagno. *Sci. Rep.* **9**, 1936 (2019).
93. A. M. Mloszewska, E. Pecoits, N. L. Cates, S. J. Mojzsis, J. O'Neil, L. J. Robbins, K. O. Konhauser, The composition of Earth's oldest iron formations: The Nuvvuagittuq Supracrustal Belt (Québec, Canada). *Earth Planet. Sci. Lett.* **317**, 331–342 (2012).
94. J. Rouillard, J. M. García-Ruiz, J. Gong, M. A. van Zuilen, A morphogram for silica-witherite biomorphs and its application to microfossil identification in the early earth rock record. *Geobiology* **16**, 279–296 (2018).
95. O. Rouxel, B. Toner, Y. Germain, B. Glazer, Geochemical and iron isotopic insights into hydrothermal iron oxyhydroxide deposit formation at Loihi Seamount. *Geochim. Cosmochim. Acta* **220**, 449–482 (2018).
96. R. M. Sherrell, M. P. Field, G. Ravizza, Uptake and fractionation of rare earth elements on hydrothermal plume particles at 9°45'N, East Pacific Rise. *East Pacific Rise. Geochim. Cosmochim. Acta* **63**, 1709–1722 (1999).
97. J. W. Schopf, V. C. Tewari, A. B. Kudryavtsev, Discovery of a new chert-permineralized microbiota in the Proterozoic Buxa Formation of the Ranjit window, Sikkim, northeast India, and its astrobiological implications. *Astrobiology* **8**, 735–746 (2008).
98. T. Suzuki, H. Hashimoto, N. Matsumoto, M. Furutani, H. Kunoh, J. Takada, Nanometer-scale visualization and structural analysis of the inorganic/organic hybrid structure of gallionella ferruginea twisted stalks. *Appl. Environ. Microbiol.* **77**, 2877–2881 (2011).
99. S. R. Taylor, S. M. McLennan, *The Continental Crust: Its Composition and Evolution* (Blackwell Scientific Publications, 1985).
100. D. Wacey, S. Menon, L. Green, D. Gerstmann, C. Kong, N. McLoughlin, M. Saunders, M. Brasier, Taphonomy of very ancient microfossils from the ~3400Ma Strelley Pool Formation and ~1900Ma Gunflint Formation: New insights using a focused ion beam. *Precambrian Res.* **220–221**, 234–250 (2012).
101. F. Widdel, S. Schnell, S. Heising, A. Ehrenreich, B. Assmus, B. Schink, ferrous iron oxidation by anoxygenic phototrophic bacteria. *Nature* **362**, 834–836 (1993).
102. A. M. Mloszewska, S. J. Mojzsis, E. Pecoits, D. Papineau, N. Dauphas, K. O. Konhauser, Chemical sedimentary protoliths in the >3.75Ga Nuvvuagittuq Supracrustal Belt (Québec, Canada). *Gondw. Res.* **23**, 574–594 (2013).
103. S. T. Krepeski, D. Emerson, P. L. Hredzak-Showalter, G. W. Luther III, C. S. Chan, Morphology of biogenic iron oxides records microbial physiology and environmental conditions: Toward interpreting iron microfossils. *Geobiology* **11**, 457–471 (2013).
104. C. Heim, N. V. Querici, D. Ionescu, N. Schafer, J. Reitner, Frutexitex-like structures formed by iron oxidizing biofilms in the continental subsurface (Åspö Hard Rock Laboratory, Sweden). *PLOS ONE* **12**, e0177542 (2017).
105. A. J. Williams, D. Y. Sumner, C. N. Alpers, S. Karunatilake, B. A. Hofmann, Preserved filamentous microbial biosignatures in the brick flat gossan, iron Mountain, California. *California. Astrobiology* **15**, 637–668 (2015).
106. M. Halbach, P. Halbach, V. Lüders, Sulfide-impregnated and pure silica precipitates of hydrothermal origin from the Central Indian Ocean. *Chem. Geol.* **182**, 357–375 (2002).
107. J. C. Alt, Hydrothermal oxide and nontronite deposits on seamounts in the eastern Pacific. *Mar. Geol.* **81**, 227–239 (1988).
108. Z. Sun, J. Li, W. Huang, H. Dong, C. T. S. Little, J. Li, Generation of hydrothermal Fe-Si oxyhydroxide deposit on the Southwest Indian Ridge and its implication for the origin of ancient banded iron formations. *J. Geophys. Res. Biogeosci.* **120**, 187–203 (2015).
109. L. Hopkinson, S. Roberts, R. Herrington, J. Wilkinson, Self-organization of submarine hydrothermal siliceous deposits: Evidence from the TAG hydrothermal mound, 26°N Mid-Atlantic ridge. *Geology* **26**, 347 (1998).
110. M. R. Walter, S. M. Awramik, Frutexitex from stromatolites of the Gunflint Iron Formation of Canada, and its biological affinities. *Precambrian Res.* **9**, 23–33 (1979).

Acknowledgments: D.P. acknowledges support from CUG-Wuhan and UCL for analytical work, Carnegie of Canada for funding field work, and Carnegie Institution for Science for access to NanoSIMS 50L. D.P. is also grateful to the municipality of Inukjuak, Québec, and the Pituvik Landholding Corporation for permission to work on their territory, and to M. Carroll for logistical support. J. Davy prepared polished thin sections and slabs used in this work, and S. Huo assisted with FIB-SEM analyses. We also thank Z. Lan, W. Martin, and M. Garcia-Ruiz for discussions that improved the manuscript and two anonymous reviewers for constructive criticism. **Funding:** Z.S. and D.P. acknowledge financial support from the National Science Foundation of China (grant no. 42172337), the Strategic Priority Research Program of the Chinese Academy of Sciences (grant no. XDB26020102), the 111 project of China (grant no.

BP0820004), and the State Key Laboratory of Biogeology and Environmental Geology (grant no. GBL12001). **Author contributions:** D.P. designed the research; performed optical microscopy, μ Raman, NanoSIMS, EA-IRMS, and FIB-SEM analyses; and wrote the manuscript. Z.S. produced the correlated μ Raman-SEM analyses. M.S.D. helped with μ Raman analyses. F.I. performed the μ CT analyses and processed FIB-BSE images. E.H. helped with NanoSIMS analyses. The manuscript received important contributions from all coauthors, except the late E.H. **Competing interests:** The authors declare that they have no competing interests. **Data**

and materials availability: All data needed to evaluate the conclusions in the paper are present in the paper and/or the Supplementary Materials.

Submitted 6 September 2021

Accepted 28 February 2022

Published 13 April 2022

10.1126/sciadv.abm2296